

Event-by-event evaluation of the prompt fission neutron spectrum from $^{239}\text{Pu}(n, f)$ R. Vogt,^{1,2} J. Randrup,³ D. A. Brown,¹ M. A. Descalle,¹ and W. E. Ormand^{1,4}¹*Physics Division, Lawrence Livermore National Laboratory, Livermore, California 94551, USA*²*Physics Department, University of California, Davis, California 95616, USA*³*Nuclear Science Division, Lawrence Berkeley National Laboratory, Berkeley, California 94720, USA*⁴*Physics Department, Michigan State University, East Lansing, Michigan 48824, USA*

(Received 23 May 2011; revised manuscript received 11 January 2012; published 13 February 2012)

Earlier studies of $^{239}\text{Pu}(n, f)$ have been extended to incident neutron energies up to 20 MeV within the framework of the event-by-event fission model FREYA, into which we have incorporated multichance fission and pre-equilibrium neutron emission. The main parameters controlling prompt fission neutron evaporation have been identified and the prompt fission neutron spectrum has been analyzed by fitting those parameters to the average neutron multiplicity $\bar{\nu}$ from ENDF-B/VII.0, including the energy-energy correlations in the covariance of $\bar{\nu}(E)$ obtained by fitting to the experimental $\bar{\nu}$ data used in the ENDF-B/VII.0 evaluation. We present our results, discuss relevant tests of this new evaluation, and describe possible further improvements.

DOI: [10.1103/PhysRevC.85.024608](https://doi.org/10.1103/PhysRevC.85.024608)

PACS number(s): 25.85.-w, 24.10.-i, 24.75.+i, 21.60.Ka

I. INTRODUCTION

Nuclear fission forms a central topic in nuclear physics, presenting many interesting issues for both experimental and theoretical research, and it has numerous practical applications as well, including energy production and security. Nevertheless, a quantitative theory of fission is not yet available. While there has been considerable progress in the last few years, both in liquid-drop model-type calculations [1,2] and in microscopic treatments [3–5], these treatments primarily address “cold” fission, induced by thermal neutrons, and cannot yet describe “hot fission,” induced by more energetic neutrons. To perform new evaluations of observables important for applications over the full relevant energy range, it is therefore necessary to rely on a considerable degree of phenomenological modeling.

One of the most important quantities for applications is the prompt fission neutron spectrum (PFNS). As discussed earlier [6], the experimental spectral data themselves are neither sufficiently accurate nor of sufficiently consistent quality to allow an improved PFNS evaluation. However, by combining measured information about the nuclear fragment yields and energies with the very precise evaluations of neutron multiplicities, it is possible to constrain the neutron spectrum rather tightly without having to rely on the spectral data themselves.

Our approach employs the fission model FREYA (Fission Reaction Event Yield Algorithm) which incorporates the relevant physics and contains a few key parameters that are determined by comparison to pertinent data through statistical analysis [6,7]. It simulates the entire fission process, starting from the possible emission of pre-equilibrium neutrons, and it generates a large sample of complete fission events with full kinematic information on the emerging fission products and the emitted neutrons and photons. FREYA provides a means of using readily measured observables to improve our understanding of the fission process and it is, therefore, a potentially powerful tool for bridging the gap between current microscopic models and important fission observables and for

improving estimates of the fission characteristics important for applications.

In the following, we briefly describe the employed version of FREYA and the fitting procedure used to obtain our extended evaluation of the $^{239}\text{Pu}(n, f)$ prompt fission neutron spectrum. We then compare our results to the ENDF-B/VII.0 [8] evaluation of the PFNS and some benchmark criticality tests. Finally, we discuss the energy and model dependence of several relevant observables.

II. GENERATION OF FISSION EVENTS

We have adapted the recently developed fission model FREYA [7] for the present purpose of calculating the neutron spectrum in terms of a set of well-defined model parameters. We describe its main physics ingredients below, with an emphasis on the new features added for the present study, particularly multichance fission and pre-equilibrium emission. Being a simulation model, FREYA follows the temporal sequence of individual fission events from the initial agitated fissionable nucleus, $^{240}\text{Pu}^*$ in the present case, through possible pre-fission emissions to a split into two excited fragments and their subsequent sequential emission of neutrons and photons. The description below is similarly organized.

A. Pre-fission neutron emission

At low-incident neutron energies, below a few MeV, the neutron is absorbed into the target nucleus resulting in an equilibrated compound nucleus which may have a variety of fates. Most frequently, in the present case, it will fission directly. But, because the compound nucleus was formed by neutron absorption, it is energetically possible for it to re-emit a neutron. In that circumstance, the daughter nucleus cannot fission and will de-excite by sequential photon emission. FREYA generally discards such events because it is designed to provide fission events (but their frequency is noted). Neutron evaporation from a fissionable compound nucleus can be

treated in the same manner as neutron evaporation from fission fragments, as will be described later (Sec. II D 1). In principle, it is also possible that the compound nucleus will start by radiating a photon but the likelihood for this is very small and is ignored.

1. Multichance fission

As the energy of the incident neutron is raised, neutron evaporation from the produced compound nucleus competes ever more favorably with direct (first-chance) fission. The associated probability is given by the ratio of the fission and evaporation widths $\Gamma_f(E^*)$ and $\Gamma_n(E^*)$ for which we use the transition-state estimate [9],

$$\frac{\Gamma_n(E^*)}{\Gamma_f(E^*)} = \frac{2g_n\mu_n\sigma \int_0^{X_n} (X_n - x)\rho_n(x)dx}{\pi\hbar^2 \int_0^{X_f} \rho_f(x)dx}, \quad (1)$$

where $g_s = 2$ is the spin degeneracy of the neutron, μ_n is its reduced mass, and $\sigma = \pi R^2 = \pi r_0^2 A^{2/3}$. Furthermore, $\rho_n(x)$ is the level density in the evaporation daughter nucleus at the excitation energy x , whose maximum value is given by $X_n = Q_n = E^* - S_n$, where Q_n is the Q value for neutron emission and S_n is the neutron separation energy. Similarly, $\rho_f(x)$ is the level density of the transition configuration for the fissioning nucleus (i.e., when its shape is that associated with the top of the fission barrier); the excitation x is measured relative to that barrier top, so its maximum value is $X_f = E^* - B_f$, where B_f is the height of the fission barrier (the corresponding quantity for neutron emission is the neutron separation energy S_n).

Neutron evaporation is possible whenever the excitation energy of the compound nucleus exceeds the neutron separation energy, $E^* > S_n$. (Because it costs energy to remove a neutron from the nucleus, S_n is positive.) The excitation energy of the evaporation daughter nucleus is $E_d^* = E^* - S_n - E$ where E is the kinetic energy of the relative motion between the emitted neutron and the daughter nucleus. If this quantity exceeds the fission barrier in the daughter nucleus, then second-chance fission is possible. (We use the Hill-Wheeler expression for the transmission probability, $P_f = 1/[1 + \exp(2\pi(B_f - E_d^*)/\hbar\omega)]$ with $\hbar\omega = 1$ MeV, so there is an exponentially small probability for sub-barrier fission.) The procedure described above is then applied to the daughter nucleus, thus making further pre-fission neutron emission possible. Thus as the incident neutron energy is raised, the emission of an ever-increasing number of pre-fission neutrons becomes possible and the associated fission events may be classified as first-chance fission (when there are no pre-fission neutrons emitted), second-chance fission (when one neutron is emitted prior to fission), and so on.

Figure 1 shows the probabilities for n^{th} -chance fission obtained with FREYA for incident neutron energies up to 20 MeV. Also shown are the GNASH results used in the ENDF-B/VII.0 evaluation [8]. The two calculations give rather similar results but, because these probabilities are not easy to measure experimentally, it is not possible to ascertain the accuracy of the calculations.

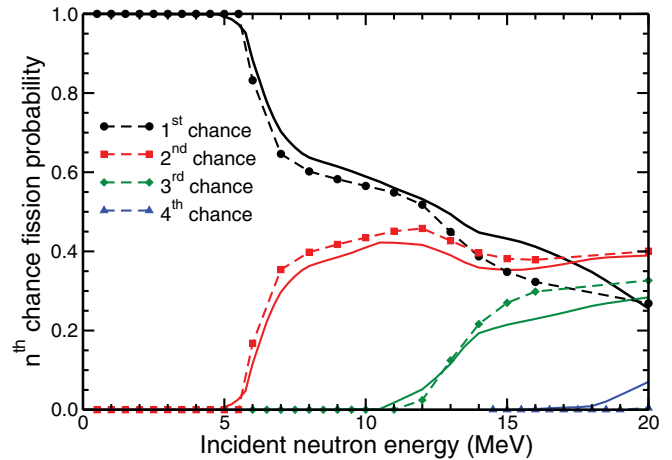


FIG. 1. (Color online) The probability for first- (black circles), second- (red squares), third- (green diamonds), and fourth- (blue triangles) chance fission as a function of incident neutron energy. The solid curves show the GNASH results used in the ENDF-B/VII.0 evaluation [8], while the dashed curves with symbols are the FREYA results discussed in the text.

2. Pre-equilibrium neutron emission

At higher incident neutron energies, there is a growing chance that complete equilibrium is not established before the first neutron is emitted. Under such circumstances the calculation of statistical neutron evaporation must be replaced by a suitable nonequilibrium treatment. A variety of models have been developed for this process (e.g., Ref. [10] which combines pre-equilibrium emission with the Madland-Nix model [11] of the prompt fission neutron spectrum). We employ a practical application of the two-component exciton model [12] (described in detail in Ref. [13]). It represents the evolution of the nuclear reaction in terms of time-dependent populations of ever more complex many-particle-many-hole states.

A given many-exciton state consists of $p_{v(\pi)}$ neutron (proton) particle excitons and $h_{v(\pi)}$ neutron (proton) hole excitons. The total number of neutron (proton) excitons in the state is $n_{v(\pi)} = p_{v(\pi)} + h_{v(\pi)}$. The incident neutron provides the initial state consisting of a single exciton, namely a neutron particle excitation: $p_v = 1$ and $p_\pi = h_v = h_\pi = 0$. In the course of time, the number of excitons present may change because of hard collisions or charge exchange, as governed by the residual two-body interaction. We ignore the unlikely accidental processes that reduce the number of excitons, so the state grows ever more complex.

The temporal development of the associated probability distribution $P(p_v, h_v, p_\pi, h_\pi)$ is described by a master equation that accounts for the transitions between different exciton states. The pre-equilibrium neutron emission spectrum is then given by

$$\frac{d\sigma_n}{dE} = \sigma_{\text{CN}} \sum_{p_\pi=0}^{p_\pi^{\text{max}}} \sum_{p_v=1}^{p_v^{\text{max}}} W(p_\pi, h_\pi, p_v, h_v, E) \times \tau(p_\pi, h_\pi, p_v, h_v) P(p_\pi, h_\pi, p_v, h_v), \quad (2)$$

where σ_{CN} is the compound nuclear cross section (usually obtained from an optical model calculation), W is the rate for emitting a neutron with energy E from the exciton state $(p_\pi, h_\pi, p_\nu, h_\nu)$, τ is the lifetime of this state, and $P(p_\pi, h_\pi, p_\nu, h_\nu)$ is the (time-averaged) probability for the system to survive the previous stages and arrive at the specified exciton state. In the two-component model, contributions to the survival probability from both particle creation and charge exchange need to be accounted for. The survival probability for the exciton state $(p_\pi, h_\pi, p_\nu, h_\nu)$ can be obtained from a recursion relation starting from the initial condition $P(p_\nu = 1, h_\nu = 0, p_\pi = 0, h_\pi = 0) = 1$ and setting $P = 0$ for terms with negative exciton number. As in Ref. [13], particle emission is assumed to occur only from states with at least three excitons, $n_\pi + n_\nu \geq 3$. We consider excitons up to $p_\nu^{\text{max}} = p_\pi^{\text{max}} = 6$.

The emission rate, $W(p_\pi, h_\pi, p_\nu, h_\nu, E_k)$, is largely governed by the particle-hole state density, $\omega(p_\pi, h_\pi, p_\nu, h_\nu, E^*)$. For a neutron ejectile of energy E the rate is given by Ref. [14]:

$$W(p_\pi, h_\pi, p_\nu, h_\nu, E_k) = \frac{g_n}{\pi^2 \hbar^3} \mu_n E \sigma_{n,\text{inv}} \frac{\omega(p_\pi, h_\pi, p_\nu - 1, h_\nu, E^* - E - S_n)}{\omega(p_\pi, h_\pi, p_\nu, h_\nu, E^*)}, \quad (3)$$

where $\sigma_{k,\text{inv}}$ is the inverse reaction cross section (calculated within the optical model framework) and E^* is the total excitation energy of the system.

The calculated probability for pre-equilibrium neutron emission is shown in the upper panel of Fig. 2 as a function of the incident neutron energy E_n , while Fig. 3 shows the pre-equilibrium neutron spectrum obtained at $E_n = 14$ MeV. After being practically negligible below a few MeV, the probability for pre-equilibrium emission grows approximately linearly to about 24% at 20 MeV. A careful inspection of the calculated energy spectrum shows that neutrons emitted from states with larger exciton number approach the statistical emission expected from a compound nucleus, thus ensuring

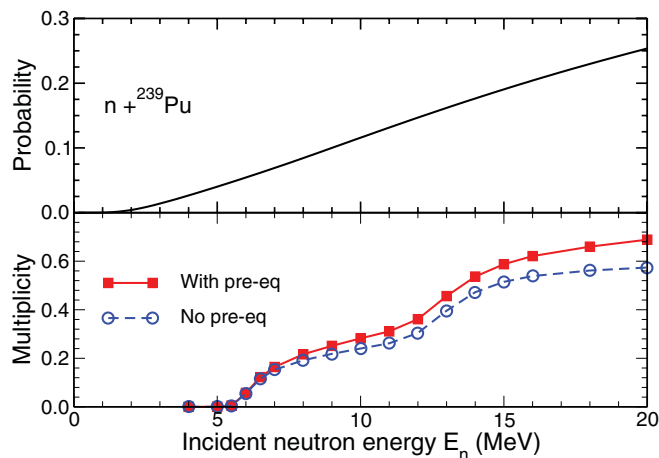


FIG. 2. (Color online) (Upper panel) The probability for pre-equilibrium neutron emission as a function of the incident neutron energy. (Lower panel) The corresponding average multiplicity of neutrons emitted prior to fission calculated without (dashed) and with (solid) the pre-equilibrium processes.

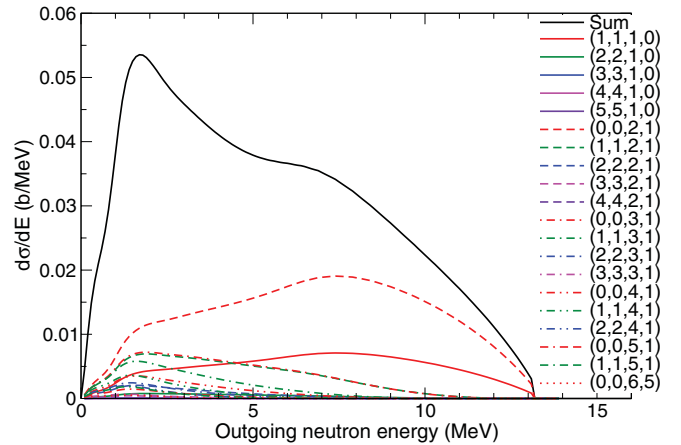


FIG. 3. (Color online) The contributions to the pre-equilibrium neutron spectrum from exciton states with the indicated values of $(p_\pi, h_\pi, p_\nu, h_\nu)$, obtained at $E_n = 14$ MeV.

our treatment has included sufficient complexity to exhaust the pre-equilibrium mechanism. Because of the (desired) insensitivity to the maximum specified exciton number, the probability shown in Fig. 2 is not indicative of the importance of the pre-equilibrium processes. Their quantitative significance is better seen by comparing the neutron multiplicity obtained with and without the pre-equilibrium treatment, as shown in the lower panel of Fig. 2.

The reaction cross sections used in Eqs. (2) and (3) define the overall magnitude of the cross sections for the pre-equilibrium processes. The highest accuracy results are best obtained from coupled-channels calculations with an appropriately determined optical potential. However, since FREYA principally deals with probabilities, the relative fraction of pre-equilibrium neutrons may be computed with sufficient accuracy employing a spherical optical potential to calculate the relevant cross sections. Consequently, the compound-nucleus cross sections and inverse cross sections were computed using the optical-model program ECIS06 and the global optical model potential of Koning and Delaroche [15].

For each event generated, FREYA first considers the possibility of pre-equilibrium neutron emission and, if it occurs, a neutron is emitted with an energy selected from the calculated pre-equilibrium spectrum (see Fig. 3). Subsequently, the possibility of equilibrium neutron evaporation is considered, starting either from the originally agitated compound nucleus, $^{240}\text{Pu}^*$, or the less excited nucleus, $^{239}\text{Pu}^*$, remaining after pre-equilibrium emission has occurred. Neutron evaporation is iterated until the excitation energy of a daughter nucleus is below the fission barrier (in which case the event is abandoned and a new event is generated) or the nucleus succeeds in fissioning.

B. Mass and charge partition

After the possible pre-fission processes, we are presented with a fission-ready compound nucleus $^{A_0}\text{Z}_0$ having an excitation energy E_0^* . The first task is to divide it into a heavy fragment $^{A_H}\text{Z}_H$ and a complementary light fragment $^{A_L}\text{Z}_L$.

Since no quantitatively useful model is yet available for the calculation of the fission fragment mass yields, we have to invoke experimental data. We follow the procedure employed in the original version of FREYA [7].

We thus assume that the mass yields $Y(A_f)$ of the fission fragments exhibit three distinct modes, each one being of Gaussian form [16],

$$Y(A_f) = S_1(A_f) + S_2(A_f) + S_L(A_f). \quad (4)$$

The first two terms represent asymmetric fission modes associated with the spherical shell closure at $N = 82$ and the deformed shell closure at $N = 88$, respectively, while the last term represents a broad symmetric mode, referred to as superlong [17]. Although the symmetric mode is relatively insignificant at low excitations, its importance increases with the excitation energy and ultimately dominates the mass distribution.

The asymmetric modes have a two-Gaussian form,

$$S_i = \frac{N_i}{\sqrt{2\pi}\sigma_i} \left[e^{-(A_f - \bar{A} - D_i)^2/2\sigma_i^2} + e^{-(A_f - \bar{A} + D_i)^2/2\sigma_i^2} \right], \quad (5)$$

while the symmetric mode is given by a single Gaussian,

$$S_L = \frac{N_L}{\sqrt{2\pi}\sigma_L} e^{-(A_f - \bar{A})^2/2\sigma_L^2}, \quad (6)$$

with $\bar{A} = \frac{1}{2}A_0$. Because each event leads to two fragments, the yields are normalized so that $\sum_A Y(A) = 2$. Thus,

$$2N_1 + 2N_2 + N_L = 2, \quad (7)$$

apart from a negligible correction because A_f is discrete and bounded from both below and above.

Most measurements are of fission *product* yields [18], the yields after prompt neutron emission is complete. However, FREYA requires fission *fragment* yields (i.e., the probability of a given mass partition before neutron evaporation has begun). While no such data are yet available for Pu, there exist more detailed data for $^{235}\text{U}(n, f)$ that give the fragment yields as functions of both mass and total kinetic energy, $Y(A_f, \text{TKE})$ for $E_n \leq 6$ MeV [19]. Guided by the energy dependence of these data, together with other available data on the product yields from $^{235}\text{U}(n, f)$ [20] and $^{239}\text{Pu}(n, f)$ [21] we derive an approximate energy dependence of the fragment yields for $^{239}\text{Pu}(n, f)$ up to $E_n = 20$ MeV.

We now discuss how we obtained the values of the parameters used in Eqs. (5) and (6). The displacements, D_i , away from symmetric fission in Eq. (5) are anchored above the symmetry point by the spherical and deformed shell closures and, because these occur at specific neutron numbers, we assume that the values of D_i are energy independent. The fitted values of the displacements for $^{235}\text{U}(n, f)$ are $D_1 = 23.05$ and $D_2 = 16.54$. The values of D_i should be smaller for ^{239}Pu than for ^{235}U , $D_i^{\text{U}} - D_i^{\text{Pu}} \approx 2$, because the larger Pu mass is closer to the shell closure locations. We take $D_1 = 20.05$ and $D_2 = 14.54$ for first-chance fission ($A_0 = 240$) and increase those values by $\frac{1}{2}$ for each pre-fission neutron emitted.

The widths of the asymmetric modes, σ_i , are expanded to second order in energy: $\sigma_i = \sigma_{i0} + \sigma_{i1}E_n + \sigma_{i2}E_n^2$. We fix the energy dependence of σ_i from the $^{235}\text{U}(n, f)$ fragment yields as a function of mass and total kinetic energy of Ref. [19]. To

adjust our results for $^{235}\text{U}(n, f)$ to $^{239}\text{Pu}(n, f)$, we assume that the general energy dependence of the parameters is the same even though the values at $E_n = 0$ are different. We find

$$\sigma_1 = 5.6 + 0.0937(E_n/\text{MeV}) + 0.034(E_n/\text{MeV})^2, \quad (8)$$

$$\sigma_2 = 2.5 + 0.11060(E_n/\text{MeV}) + 0.008(E_n/\text{MeV})^2. \quad (9)$$

When the fissioning nucleus is the original system, ^{240}Pu , then E_n is the value of the actual incident neutron energy. But when the fissioning nucleus is lighter (i.e., when ν_0 pre-fission neutrons have been emitted), then E_n is the equivalent incident neutron energy, that is, the incident energy that would generate the given excitation energy E_0^* when absorbed by the nucleus $^{239-\nu_0}\text{Pu}$. The width of the superlong component, σ_L , is assumed to be constant, independent of both the incident energy and the fissioning isotope. We take $\sigma_L = 12$.

The normalizations N_i change only slowly with incident energy until symmetric fission becomes more probable, after which they decrease rapidly. We therefore model the energy dependence of N_i by a Fermi distribution,

$$N_i = N_i^0 (1 + \exp[(E_n - E_1)/E_2])^{-1}. \quad (10)$$

We assume that the midpoint and the width are the same for both modes, $E_1 = 10.14$ MeV and $E_2 = 1.15$ MeV, so that the relative normalizations for the asymmetric modes have the same energy dependence. We have not assumed that E_1 and E_2 are identical for U and Pu because the transition from asymmetric to more symmetric fission is not as smooth a function of energy in the few-MeV region for Pu as it is for U [20,21]. We take $N_1^0 = 0.757$ and $N_2^0 = 0.242$. With N_1 and N_2 given by Eq. (10), N_L is determined from Eq. (7).

The resulting fragment yields for two representative incident neutron energies are shown in Fig. 4. The deep dip at $\frac{1}{2}A_0$ visible for the thermal yields has substantially filled in by $E_n = 14$ MeV. The fragment yield at 14 MeV is a composite distribution because there are substantial contributions from second- and third-chance fission for incident neutrons of such high energy (see Fig. 1). The dashed curve in Fig. 4 includes these contributions weighted with the appropriate probabilities shown in Fig. 1.

The overall broadening of the yields is caused by a combination of two effects: the larger widths of the S_1 and S_2 modes at higher energies and the increased contribution of the S_L component. We note that while σ_L does not change, the larger N_L enhances the importance of this component.

Once the Gaussian fit has been performed, it is straightforward to make a statistical selection of the fragment mass number A_f . The mass number of the partner fragment is then readily determined since $A_L + A_H = A_0 - \nu_0$.

The fragment charge Z_f is selected subsequently. For this we follow Ref. [22] and employ a Gaussian form,

$$P_{A_f}(Z_f) \propto e^{-(Z_f - \bar{Z}_f(A_f))^2/2\sigma_Z^2}, \quad (11)$$

with the condition that $|Z_f - \bar{Z}_f(A_f)| \leq 5\sigma_Z$. The centroid is determined by requiring that the fragments have, on average, the same charge-to-mass ratio as the fissioning nucleus, $\bar{Z}_f(A_f) = A_f Z_0/A_0$. The dispersion is the measured value, $\sigma_Z = 0.5$ [22]. The charge of the complementary fragment then follows using $Z_L + Z_H = Z_0$.

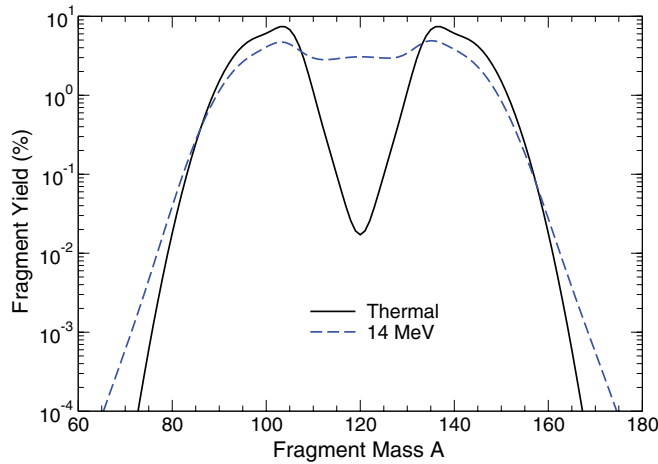


FIG. 4. (Color online) Calculated fragment yields as a function of fragment mass for thermal (solid) and 14 MeV (dashed) neutrons. The 14 MeV result also includes contributions from multichance fission events.

C. Fragment energies

Once the partition of the total mass and charge between the two fragments has been selected, the Q value associated with that particular fission channel follows as the difference between the total mass of the fissioning nucleus and the ground-state masses of the two fragments,

$$Q_{LH} = M(^{240-^{241}}\text{Pu}^*) - M_L - M_H. \quad (12)$$

FREYA takes the required nuclear ground-state masses from the compilation by Audi *et al.* [23], supplemented by the calculated masses of Möller *et al.* [24] when no data are available. The Q_{LH} value for the selected fission channel is then divided up between the total kinetic energy (TKE) and the total excitation energy (TXE) of the two fragments. The specific procedure employed is described below.

Through energy conservation, the total fragment kinetic energy TKE is intimately related to the resulting combined multiplicity of evaporated neutrons, $\nu_L + \nu_H$, which needs to be obtained very accurately.

Figure 5 shows the measured average TKE value as a function of the mass number of the heavy fragment A_H . Near symmetry, the plutonium fission fragments are midshell nuclei subject to strong deformations. Thus the scission configuration will contain significant deformation energy and a correspondingly low TKE. At $A_H = 132$, the heavy fragment is close to the doubly magic closed shell having $Z_H = 50$ and $N_H = 82$ and is therefore resistant to distortions away from sphericity, as first discussed in Ref. [25]. Consequently, the scission configuration is fairly compact, causing the TKE to exhibit a maximum even though the complementary light fragment is far from a closed shell and hence significantly deformed.

The TKE values shown in Fig. 5 were obtained in experiments using thermal neutrons [26–28]. Unfortunately, there are no such data for higher incident energy. We therefore assume the energy-dependent average TKE values take the

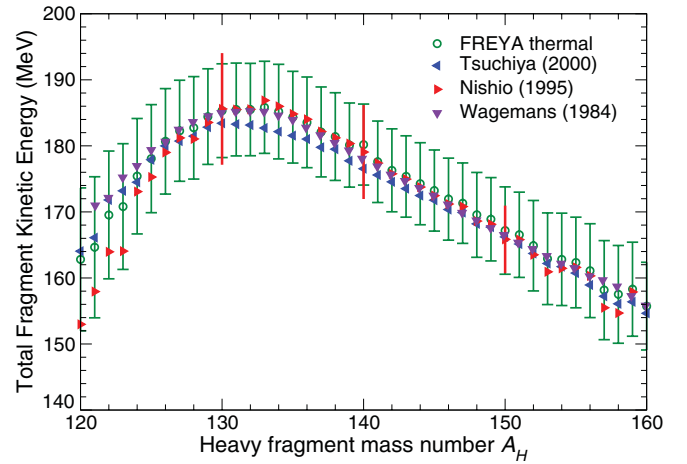


FIG. 5. (Color online) The measured average TKE as a function of the mass number of the heavy fragment [26–28] compared to FREYA calculations at thermal energies. The FREYA result is shown with the calculated dispersion around each A_H .

form

$$\overline{\text{TKE}}(A_H, E_n) = \overline{\text{TKE}}_{\text{data}}(A_H) + d\text{TKE}(E_n). \quad (13)$$

The first term is extracted from the data shown in Fig. 5, while the second term is a parameter adjusted to ensure reproduction of the measured energy-dependent average neutron multiplicity $\bar{\nu}(E_n)$. In each particular event, the actual TKE value is then obtained by adding a thermal fluctuation to the above average, as explained later.

Figure 5 includes the average TKE values calculated with FREYA at thermal energies, together with the associated dispersions (these bars are *not* sampling errors but indicate the actual width of the TKE distribution for each A_H).

Figure 6 shows the single-fragment kinetic energy obtained with FREYA for incident thermal neutrons. Although FREYA is not explicitly tuned to match the single-fragment kinetic

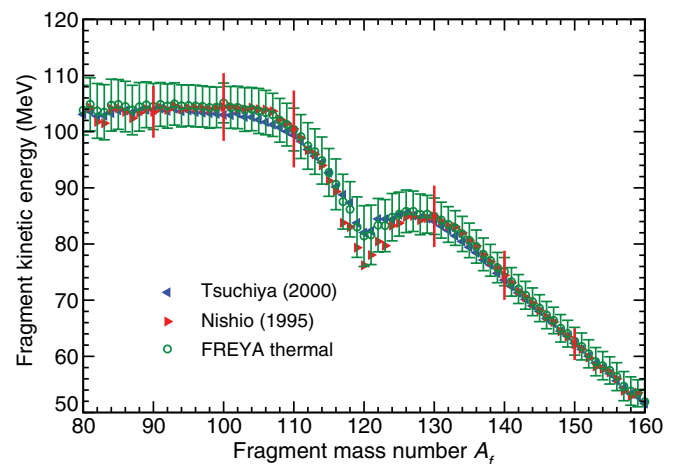


FIG. 6. (Color online) The average fragment kinetic energy as a function of fragment mass from Refs. [27,28] compared to FREYA calculations at thermal energies. The FREYA result is shown with the calculated dispersion around each A_f .

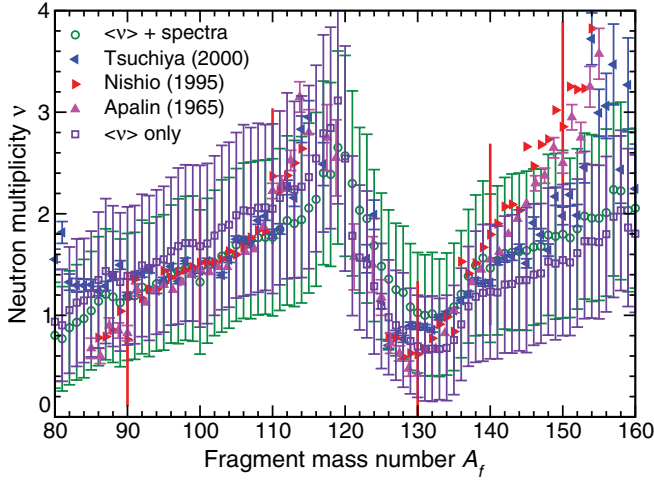


FIG. 7. (Color online) The measured average neutron multiplicity as a function of the fragment mass [27–29] together with the FREYA average and dispersions indicated for each A_f fitting to $\bar{\nu}$ only (squares) and with the spectra included in the fit (circles).

energies, it does reproduce these data quite well, as would be expected from momentum conservation. The light fragment carries away significantly more kinetic energy than the heavy fragment. Furthermore, the kinetic energy of the fragment is nearly constant for $A_f < 106$, but after the dip near symmetry there is an approximately linear decrease in the fragment kinetic energy. The figure also shows the calculated width in the fragment energy distribution, together with a few typical experimental widths provided by Ref. [27].

Of particular interest is the dependence of the average neutron multiplicity on the fragment mass number A_f , shown in Fig. 7. It is seen that the FREYA calculations provide a rather good representation of the “sawtooth” behavior of $\bar{\nu}(A_f)$, as shown in Fig. 7, even though FREYA is also not tuned to these data. This is not particularly surprising because we have adopted the shape of $\text{TKE}(A_H)$ in Fig. 5. The dip in the calculation and the data at $A \sim 132$ is at the same point as the peak of $\text{TKE}(A_H)$ due to the shell-driven fragment deformation pointed out in Ref. [25]. Although the agreement is good, the observed behavior is not perfectly reproduced. When $A_f > 150$, a region where the fragment yield is decreasing sharply, the data and the calculations appear to diverge. We note that the uncertainties on the data in this region, where reported, are rather large.

Once the average total fragment kinetic energy has been obtained, the average combined excitation energy in the two fragments follows by energy conservation,

$$\overline{\text{TXE}} = \bar{E}_L^* + \bar{E}_H^* \doteq Q_{LH} - \overline{\text{TKE}}. \quad (14)$$

The first relation indicates that the total excitation energy is partitioned between the two fragments. As is common, we assume that the fragment level densities are of the form $\rho_i(E_i^*) \sim \exp(2\sqrt{a_i U_i})$, where U_i is the effective statistical energy in the fragment.

We have used a description of the level-density parameter based on the back-shifted Fermi gas (BSFG) model [30],

$$a_i(E_i^*) = \frac{A_i}{e_0} \left[1 + \frac{\delta W_i}{U_i} (1 - e^{-\gamma U_i}) \right], \quad (15)$$

where $U_i = E_i^* - \Delta_i$ and $\gamma = 0.05$, also used in Ref. [31]. The pairing energy of the fragment Δ_i and its shell correction δW_i are tabulated in Ref. [30] based on the mass formula of Koura *et al.* [32]. If δW_i is negligible or if U is large then the renormalization of a_i is immaterial and the BSFG level-density parameter reverts to the simple form, $a_i \approx A_i/e_0$.¹ [Because the back shift causes U_i to become negative when E_i^* is smaller than Δ_i , we replace $U_i(E_i^*)$ by a quadratic spline for $E_i^* \leq 2\Delta_i$ while retaining the expressions $T_i = \sqrt{U_i/a_i}$ for the temperature and $\sigma_{E_i^*}^2 = 2U_i T_i$ for the variance of the energy distribution to ensure a physically reasonable behavior.] We take e_0 as an adjustable model parameter.

If the two fragments are in mutual thermal equilibrium, $T_L = T_H$, the total excitation energy will, on average, be partitioned in proportion to the respective heat capacities which in turn are proportional to the level-density parameters (i.e., $\bar{E}_i^* \sim a_i$). FREYA therefore first assigns tentative average excitations based on such an equipartition,

$$\dot{E}_i^* = \frac{a_i(\tilde{E}_i^*)}{a_L(\tilde{E}_L^*) + a_H(\tilde{E}_H^*)} \overline{\text{TXE}}, \quad (16)$$

where $\tilde{E}_i^* = (A_i/A_0)\overline{\text{TXE}}$. Subsequently, because the observed neutron multiplicities suggest that the light fragments tend to be disproportionately excited, the average values are adjusted in favor of the light fragment,

$$\bar{E}_L^* = x \dot{E}_L^*, \quad \bar{E}_H^* = \overline{\text{TKE}} - \bar{E}_L^*, \quad (17)$$

where x is an adjustable model parameter expected to be larger than unity, as suggested by measurements of $^{235}\text{U}(n,f)$ [33] and $^{252}\text{Cf}(sf)$ [34].

After the mean excitation energies have been assigned, FREYA considers the effect of thermal fluctuations. The fragment temperature T_i is obtained from $\bar{U}_i \equiv U_i(\bar{E}_i^*) = a_i T_i^2$ and the associated variance in the excitation E_i^* is taken as $\sigma_i^2 = 2\bar{U}_i^* T_i$, where $U(E^*) = E^*$ in the simple (unshifted) scenario.

Therefore, for each of the two fragments, we sample a thermal energy fluctuation δE_i^* from a normal distribution of variance σ_i^2 and modify the fragment excitations accordingly, arriving at

$$E_i^* = \bar{E}_i^* + \delta E_i^*, \quad i = L, H. \quad (18)$$

Energy conservation requires a compensating opposite fluctuation in the total kinetic energy, so that

$$\text{TKE} = \overline{\text{TKE}} - \delta E_L^* - \delta E_H^*. \quad (19)$$

With both the excitations and the kinetic energies of the two fragments fully determined, it is an elementary matter to calculate the magnitude of the momenta with which they

¹This form, used by Madland and Nix [11], is independent of excitation energy.

emerge after having been fully accelerated by their mutual Coulomb repulsion [7]. The fission direction is assumed to be isotropic (i.e., directionally random) in the frame of the fissioning nucleus and the resulting fragment velocities are finally Lorentz boosted into the rest frame of the original $^{240}\text{Pu}^*$ system.

D. Fragment de-excitation

Usually both fully accelerated fission fragments are excited sufficiently to permit the emission of one or more neutrons. We simulate the evaporation chain in a manner conceptually similar to the method of Lemaire *et al.* [31] for $^{252}\text{Cf}(sf)$ and $^{235}\text{U}(n, f)$. After neutron emission is no longer energetically possible, FREYA simulates the sequential emission of photons by a similar method [7] (see also Ref. [35]).

1. Neutron evaporation

Neutron emission is treated by iterating a simple neutron evaporation procedure for each of the two fragments separately. At each step in the evaporation chain, the excited mother nucleus $^A_i Z_i$ has a total mass equal to its ground-state mass plus its excitation energy, $M_i^* = M_i^{\text{gs}} + E_i^*$. The Q value for neutron emission from the fragment is then $Q_n = M_i^* - M_f - m_n$, where M_f is the ground-state mass of the daughter nucleus and m_n is the mass of the neutron. (For neutron emission we have $A_f = A_i - 1$ and $Z_f = Z_i$.) The Q value is equal to the maximum possible excitation energy of the daughter nucleus, achieved if the final relative kinetic energy vanishes. The temperature in the daughter fragment is then maximized at T_f^{max} . Thus, once Q_n is known, the kinetic energy of the evaporated neutron may be sampled. FREYA assumes that the angular distribution is isotropic in the rest frame of the mother nucleus and uses a standard spectral shape [36],

$$f_n(E) \equiv \frac{1}{N_n} \frac{dN_n}{dE} \sim E e^{-E/T_f^{\text{max}}}, \quad (20)$$

which can be sampled efficiently [7].

Although relativistic effects are very small for neutron evaporation, they are taken into account to ensure exact conservation of energy and momentum, which is convenient for code verification purposes. We therefore take the sampled energy E to represent the *total* kinetic energy in the rest frame of the mother nucleus (i.e., it is the kinetic energy of the emitted neutron *plus* the recoil energy of the excited residual daughter nucleus). The daughter excitation is then given by

$$E_d^* = Q_n - E, \quad (21)$$

and its total mass is thus $M_d^* = M_d^{\text{gs}} + E_d^*$. The magnitude of the momenta of the excited daughter and the emitted neutron can then be determined [7]. Sampling the direction of their relative motion isotropically, we thus obtain the two final momenta which are subsequently boosted into the overall reference frame by the appropriate Lorentz transformation.

This procedure is repeated until no further neutron emission is energetically possible (i.e., when $E_d^* < S_n$), where S_n is the

neutron separation energy in the prospective daughter nucleus, $S_n = M(^{A_d}Z_d) - M(^{A_d-1}Z_d) - m_n$.

2. Photon radiation

After the neutron evaporation has ceased, the excited product nucleus may de-excite by sequential photon emission. FREYA treats this process in a manner analogous to neutron evaporation (i.e., as the statistical emission of massless particles). While this simple treatment is expected to be fairly reasonable at the early stage where the level density can be regarded as continuous, it would obviously be inadequate for late stages that involve transitions between specific levels.

There are two important technical differences relative to the treatment of neutron emission. There is no separation energy for photons and, because they are massless, there is no natural end to the photon emission chain. We therefore introduce an infrared cutoff of 200 keV. Whereas the neutrons may be treated by nonrelativistic kinematics, the photons are ultrarelativistic. As a consequence, their phase space has an extra energy factor,

$$f_\gamma(E) \equiv \frac{1}{N_\gamma} \frac{dN_\gamma}{dE} \sim E^2 e^{-E/T_f^{\text{max}}}. \quad (22)$$

The photons are assumed to be emitted isotropically and their energy can be sampled very quickly from the above photon energy spectrum [7]. The procedure is repeated until the available energy is below the specified cutoff, yielding a number of kinematically fully-characterized photons for each of the product nuclei.

III. RESULTS

We now proceed to discuss our analysis of the prompt fission neutron spectrum (PFNS). We first describe the computational approach and then explain how the model parameters are determined. The resulting prompt neutron spectral evaluations are then discussed in detail. Finally, we present some additional observables of particular relevance.

A. Computational approach

Here we briefly describe the statistical method used for determining model parameters and reaction observables. Our analysis uses the Monte Carlo approach to Bayesian inference outlined in many books on general inverse problem theory (e.g., Ref. [37]).

We have introduced several model parameters: e_0 , x , and $d\text{TKE}$, which in principle may be adjusted for each incident neutron energy E_n . However, because independent fits to the experimental data tend to yield values of e_0 and x that are nearly independent of E_n [6], we shall assume that these two parameters are energy independent. This simplification will facilitate the optimization procedure. Thus a given model realization is characterized by the two values e_0 and x together with the function $d\text{TKE}(E_n)$ which, for practical purposes, will be defined by its values at certain selected energies, $\{d\text{TKE}_\ell\}$.

For formal convenience, we denote the set of model parameter values as $\mathbf{m} = \{m_k\}$.

When FREYA is used with any particular value set \mathbf{m} , it yields a sample of fission events from which we can extract observables $\mathbf{d}(\mathbf{m})$ that can be directly compared to the corresponding experimental values \mathbf{d}_{exp} . For example, we may extract the energy-dependent mean neutron multiplicity $\bar{\nu}(E_n)$, and compare it with the values given in the ENDF/B-VII.0 evaluation [8].

We assume that the experiment provides not just the values but also the entire associated covariance matrix Σ_{exp} . (The square roots of the diagonal elements of Σ_{exp} are the uncertainties on the individual observables.) The degree to which the particular model realization defined by the parameter values \mathbf{m} describes the measured data \mathbf{d}_{exp} is then expressed by

$$P(\mathbf{d}_{\text{exp}}|\mathbf{m}) \sim \exp\left(-\frac{1}{2}\chi^2(\mathbf{m})\right), \quad (23)$$

where $\chi^2(\mathbf{m})$ is the generalized least-squares deviation between the model \mathbf{m} and experiment,

$$\chi^2 = (\mathbf{d}_{\text{exp}} - \mathbf{d}(\mathbf{m})) \cdot (\Sigma_{\text{exp}})^{-1} \cdot (\mathbf{d}_{\text{exp}} - \mathbf{d}(\mathbf{m}))^T. \quad (24)$$

Employing merely the diagonal part of Σ_{exp} (i.e., the uncertainties alone) ensures that well-measured observables carry more weight than poorly measured ones. This approach was used in the previous PFNS evaluation [6], which was restricted to lower energy ($E_n < 5.5$ MeV). Here we now employ the full covariance matrix, thereby ensuring that correlations between measured observables are also taken into account. As we shall see, these correlations do impact the results.

Using the above framework, we may now compute the weighted averages of arbitrary observables $\mathcal{O} = \{\mathcal{O}_i\}$. We assume that the physically reasonable values of the model parameters \mathbf{m} are uniformly distributed within a hypercube in parameter space. This defines the *a priori* model probability distribution $P(\mathbf{m})$. The *best estimate* of the observable \mathcal{O}_i is then given by

$$\langle \mathcal{O}_i \rangle = \int d\mathbf{m} P(\mathbf{m}) P(\mathbf{d}_{\text{exp}}|\mathbf{m}) \mathcal{O}_i(\mathbf{m}). \quad (25)$$

The best estimate for the covariance between two such observables can be obtained similarly,

$$\begin{aligned} \mathcal{O}_{ij} &\equiv \langle \mathcal{O}_i \mathcal{O}_j \rangle - \langle \mathcal{O}_i \rangle \langle \mathcal{O}_j \rangle \\ &= \langle \mathcal{O}_i - \langle \mathcal{O}_i \rangle \rangle \langle \mathcal{O}_j - \langle \mathcal{O}_j \rangle \rangle. \end{aligned} \quad (26)$$

In particular, we may compute the best estimate of $\bar{\nu}$,

$$\langle \bar{\nu} \rangle = \int d\mathbf{m} P(\mathbf{m}) P(\mathbf{d}_{\text{exp}}|\mathbf{m}) \bar{\nu}(\mathbf{m}), \quad (27)$$

and the prompt neutron spectrum, as well as the covariances between those quantities.

In practice, we average over parameter space employing a Monte Carlo approach, thereby reducing the integral over all possible parameter values \mathbf{m} to a sum over N sampled model realizations, $\{\mathbf{m}^{(n)}\}$,

$$\langle \mathcal{O}_i \rangle \approx \frac{1}{N} \sum_{n=1}^N P(\mathbf{m}^{(n)}) P(\mathbf{d}_{\text{exp}}|\mathbf{m}^{(n)}) \mathcal{O}_i(\mathbf{m}^{(n)}). \quad (28)$$

The joint probability $w_n \equiv P(\mathbf{m}^{(n)})P(\mathbf{d}_{\text{exp}}|\mathbf{m}^{(n)})$ may be viewed as the likelihood that the particular model realization $\mathbf{m}^{(n)}$ is ‘‘correct.’’ Because it depends exponentially on χ_n^2 , the likelihood tends to be strongly peaked around the favored set. It is important that the parameter sample be sufficiently dense in the peak region to ensure that many sets have non-negligible weights. We use Latin Hypercube sampling (LHS) [38,39], which samples a function of K variables with the range of each variable divided into M equally spaced intervals. Each combination of M and K is sampled at most once, with a maximum number of combinations being $(M!)^{K-1}$. The LHS method generates samples that better reflect the distribution than a purely random sampling would. Consequently, relative to a simple Monte Carlo sampling, the employed sampling method requires fewer realizations to determine the optimal parameter set. We used 5000 realizations of the parameter space to obtain the optimal parameter values.

Even though both $\bar{\nu}$ and the neutron spectrum are important observables, the small uncertainties on the evaluated $\bar{\nu}$ drive the results. Indeed, for our primary result, we use only the evaluated $\bar{\nu}$ to constrain our new evaluation of the PFNS, as in Ref. [6]. Thus, in this treatment, the spectra is an outcome rather than a comparative observable. We use the evaluated $\bar{\nu}$ in the ENDF/B-VII.0 database [8] with the covariance resulting from the least-squares fit to the available $^{239}\text{Pu}(n, f)$ data described in Ref. [40]. The energy-dependent neutron multiplicity, $\bar{\nu}(E_n)$ is represented as a locally linear fit to the experimental data. Because the nodes in this fit do not align with fitted data, the fit introduces energy correlations that are encoded into the covariance matrix.

To show the difference in the resulting evaluation when the spectral data are included, we also present a fit to $\bar{\nu}$ and spectral data themselves. Because the data are often given with an arbitrary normalization, we normalize them to unity while preserving their spectral shapes, following the prescription of Ref. [6]. We note that this procedure could introduce some bias into the result because a particular functional form has been assumed to obtain the integral normalization. In addition, these data are primarily for incident neutrons from thermal energies up to 0.5 MeV [41–49] although one group reported results for incident neutron energies up to 3.5 MeV [49]. Because the shape of the data reported in Ref. [48] is significantly different from the other data, they were not included in the fit.

For each model realization, FREYA is used to generate a large sample of fission events (typically one million events for each parameter set) for each of the selected incident neutron energies and the resulting average multiplicity $\bar{\nu}(E_n)$ is extracted from the generated event sample.

B. Fit results

Given the tendency of e_0 to be larger than 8 MeV, we let e_0 vary between 8 and 12 MeV. In addition, recalling our previous results [6] and the experimental indications that the light fragment is hotter than the heavy fragment, we have assumed $1 \leq x \leq 1.4$. The resulting optimal values of these parameters are $e_0 = 9.2648 \pm 0.0453$ MeV and $x = 1.2449 \pm 0.0066$ when fitting to $\bar{\nu}$ only and $e_0 = 9.6905 \pm 0.3441$ MeV and

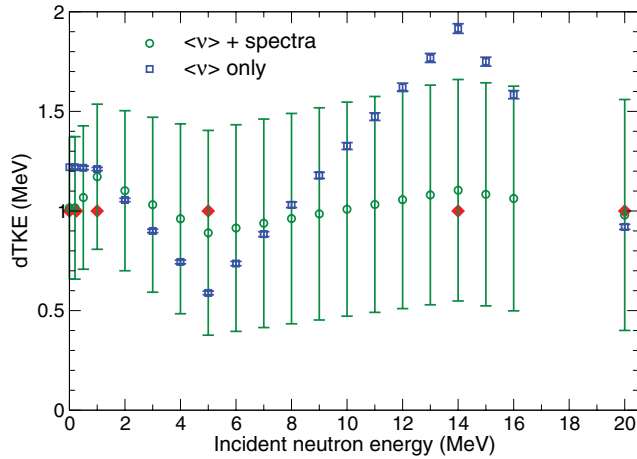


FIG. 8. (Color online) The values of $dTKE$ and the associated fit uncertainty as a function of incident neutron energy obtained when fitting to $\bar{\nu}$ alone (squares) and to $\bar{\nu}$ and the spectral data (circles). The locations of the node points are indicated by diamonds at $dTKE = 1$ MeV.

$x = 1.0536 \pm 0.0445$ when the spectra are included. These values of e_0 are consistent with the calculation of a in Eq. (15) which does not include collective effects. If collective behavior is included, then we expect $e_0 \sim 13$ MeV based on the RIPL-3 systematics [50]. Previously, we obtained $e_0 \sim 8$ MeV and $x \sim 1.1$ with a slightly different TKE prescription and using only the diagonal elements of the $\bar{\nu}$ covariance matrix [6].

We have fitted $dTKE$ at six values of incident neutron energy, $E_n = 10^{-11}$, 0.25, 1, 5, 14, and 20 MeV, to keep the parameter space manageable. These points are chosen to reflect the physics of the fission process: The region between 0.25 and 1 MeV is where $\bar{\nu}(E_n)$ changes slope while the second-chance fission threshold is just above 5 MeV. The full 20-point grid of the FREYA evaluation is then covered by means of a linear interpolation between these node points. The resulting values of $dTKE$ for both fits are shown in Fig. 8. The locations of the node points are indicated by diamonds at $dTKE = 1$ MeV. The error bars on $dTKE$ at the node points are the standard deviations obtained from the averaging over the range of parameter values while the error bars on $dTKE$ between two node points are the interpolated dispersions between those two points. Note the large uncertainties associated with including the spectra in the fit relative to those obtained by fitting to $\bar{\nu}$ alone. A similar difference in the uncertainties on e_0 and x can also be observed.

Because $dTKE$ represents the shift in the total fragment kinetic energy from the value obtained for incident thermal neutron energies, $dTKE$ should depend on the incident neutron energy, as suggested in Eq. (13). The value of $dTKE$ is positive, indicating that using the thermal average value of TKE leads to too many neutrons. The positive $dTKE$ is then required to reduce the excitation energy sufficiently to give a good fit to $\bar{\nu}$. For example, reducing $dTKE$ at $E_n = 0.5$ MeV from 1.1 MeV to zero while retaining the same values of e_0 and x , reduces the peak value of $\overline{TKE}(A_H)$ by about 0.6% while increasing $\bar{\nu}$ by $\sim 5\%$.

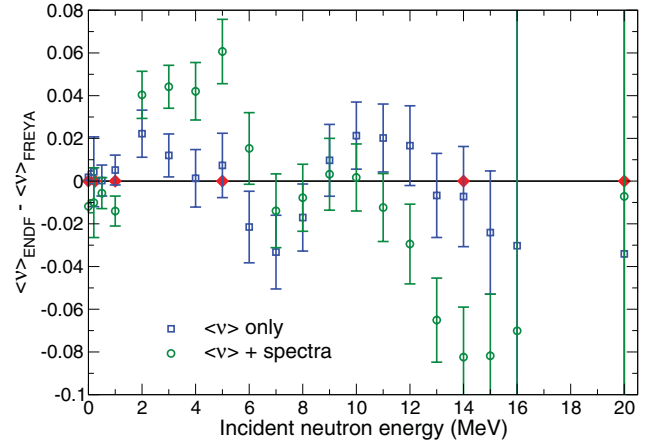


FIG. 9. (Color online) The residual differences between the ENDF-B/VII.0 evaluation and our fits for $\bar{\nu}$ only (squares) and $\bar{\nu}$ with the spectral data (circles) using FREYA. The locations of the node points are indicated by diamonds at $\langle \nu \rangle_{\text{ENDF}} - \langle \nu \rangle_{\text{FREYA}} = 0$. The uncertainty on the residual only reflects the uncertainty on $\bar{\nu}$ from the ENDF-B/VII.0 evaluation.

We can test the sensitivity of $\bar{\nu}$ to changes in the parameter values by changing one parameter while keeping the other two fixed. For example, reducing $dTKE$ by 10% increases $\bar{\nu}$ by 0.55% while decreasing x by 10% decreases $\bar{\nu}$ by 0.1%. The largest change in $\bar{\nu}$ arises when e_0 drops by 10%. In this case, $\bar{\nu}$ is 0.86% larger.

Above 14 MeV, the ENDF-B-VII.0 $\bar{\nu}$ evaluation is not based on data but on a linear extrapolation of measurements taken at lower incident energies. Thus, $\bar{\nu}$ is not well constrained near the high end of the energy range.

A direct comparison of our fitted values of $\bar{\nu}$ with those in the ENDF-B/VII.0 evaluation is less revealing than fit residuals, the difference $\bar{\nu}_{\text{ENDF}} - \bar{\nu}_{\text{FREYA}}$. The residual values are shown in Fig. 9. The standard deviation on each point reflects only the uncertainty on the ENDF-B/VII.0 evaluation and not the uncertainty on the fitted $\bar{\nu}$. The large uncertainties at 16 and 20 MeV arise from the lack of experimental data at these values of E_n .

We note that the ENDF-B/VII.0 $\bar{\nu}$ evaluation lies more than one standard deviation above the evaluated $\bar{\nu}$ data extracted in the ENDF-B/VII.0 covariance analysis in the region $0.1 < E_n < 1$ MeV [40]. Our results agree rather well with the evaluated data in this region. Here, where $\bar{\nu}$ is smallest, the relative difference is less than 0.5%, even when the spectra are included in the fit. The residual difference is largest when $E_n > 12$ MeV. When we fit to $\bar{\nu}$ alone, the differences are much smaller. Note that the finite residuals arise because we have taken the energy-energy correlations in the $\bar{\nu}$ evaluation into account. If we would assume, as in our previous work [6], that the value of $\bar{\nu}$ at each energy point is independent of all others (e.g., the errors are uncorrelated and the covariance matrix is diagonal), then the fit residuals can be very small.

Examples of the resulting prompt fission neutron spectrum are shown in Fig. 10. We present $d\nu/dE$ for four representative energies: $E_n = 0.5$ MeV (thermal neutrons), 4 MeV (below the second-chance fission threshold), 9 MeV (below the threshold

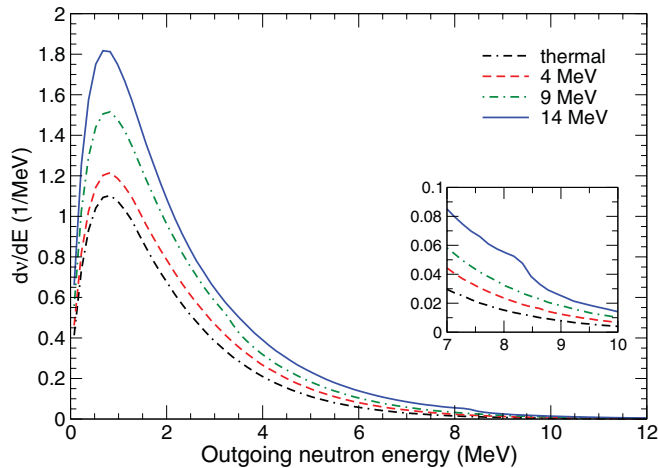


FIG. 10. (Color online) The prompt neutron spectra resulting from our fits, at selected values of E_n . The inset emphasizes the change in slope due to pre-fission neutron emission at 8.4 MeV for $E_n = 14$ MeV.

for third-chance fission), and 14 MeV (relevant for certain experimental tests). We note that the integral of dv/dE over outgoing neutron energies gives the average neutron multiplicity, $\bar{\nu}$, obtained from the fitting procedure. In addition to the increase in the peak of the spectrum, we note that the average outgoing neutron energy appears to increase with incident energy.

A close inspection of the spectra obtained for 9 and 14 MeV will reveal abrupt drops in value at the energies corresponding to the threshold for emission of a second pre-fission neutron, namely, at $\hat{E}_2 = E_n - S_n(^{239}\text{Pu})$, 3.4 and 8.4 MeV, respectively. The inset of Fig. 10 emphasizes the threshold at 8.4 MeV. When the energy of the first pre-fission neutron is below \hat{E}_2 , the daughter nucleus is sufficiently excited to make secondary emission possible. (These threshold discontinuities are also visible in the spectral differences shown in Figs. 12 and 13.) This effect, noted already by Kawano *et al.* [10], grows larger at higher incident energies where multichance fission is more probable. Furthermore, when the combined energy of the first two pre-fission neutrons is below $\hat{E}_3 = E_n - S_n(^{239}\text{Pu}) - S_n(^{238}\text{Pu})$ the emission of a third pre-fission neutron is energetically possible. In principle, these onset effects can be measured experimentally which could thus provide novel quantitative information on the degree of multichance fission.

Figure 11 compares the spectral results from the two fits at $E_n = 0.5$ and 14 MeV. Because the differences are largest in the high-energy tail, we have placed the curves on a semilog scale to demonstrate the differences more clearly. It is clear that the spectra fit to $\bar{\nu}$ alone are hotter.

Our final evaluation is based on our fits to $\bar{\nu}$ and its energy-energy covariance, either with or without fitting the spectra also, as described above. The resulting spectral evaluations are incorporated in different ENDF-type files with their spectral shapes alone.

To produce the spectral evaluation, requiring fine energy spacings over the range $10^{-5} \leq E \leq 20$ MeV, from our FREYA

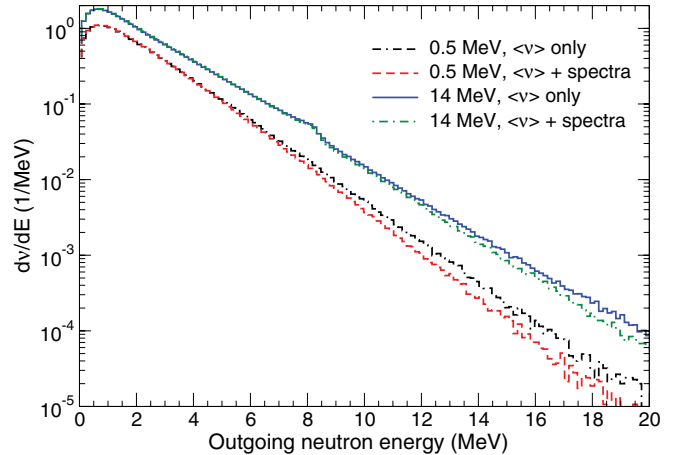


FIG. 11. (Color online) Comparison of the prompt neutron spectra at incident neutron energies of 0.5 and 14 MeV resulting from the fits to $\bar{\nu}$ alone and including the spectral data. The results are shown on a semilog scale to emphasize the high-energy tails of the spectra.

results, we fit the FREYA PFNS in the regions where either the employed bin widths are not sufficiently small (in the region below 0.1 MeV) or the statistics are limited (above 6–8 MeV). In between, we interpolate the FREYA spectra. We also interpolate the spectra around the multichance fission thresholds where smooth fitting would not be appropriate.

Figures 12 and 13 give the difference between the present evaluations and the ENDF/B-VII.0 evaluation. The spectra are all normalized to unity at each value of E_n . In both cases, for incident neutron energies below the threshold for multichance fission, the difference between ENDF/B/VII.0 and our evaluations is around 1% for $E < 0.1$ MeV, fluctuating to $\pm 10\%$ between 0.1 and 10 MeV. In most cases, the percent difference between the two evaluations is rather small, less

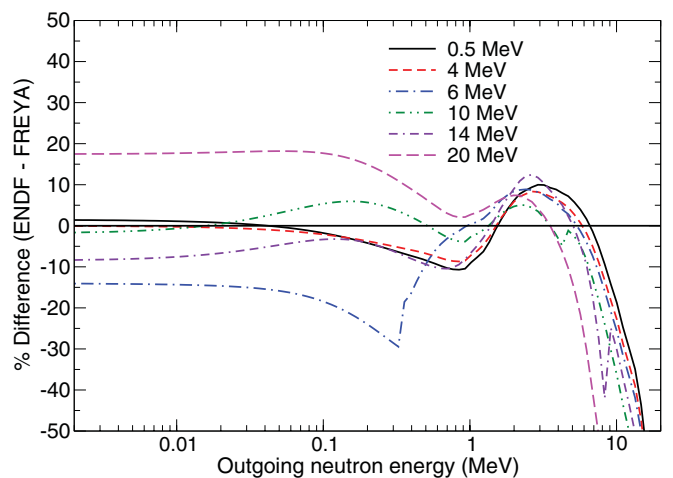


FIG. 12. (Color online) The percent difference between the ENDF/B/VII.0 evaluation of the PFNS and our resulting fit to $\bar{\nu}$ only at several representative incident neutron energies. Results are shown for 0.5 (solid black), 4 (short dashed red), 6 (dot-dashed blue), 10 (dot-dot-dashed green), 14 (dot-dash-dashed violet), and 20 (long dashed magenta) MeV.

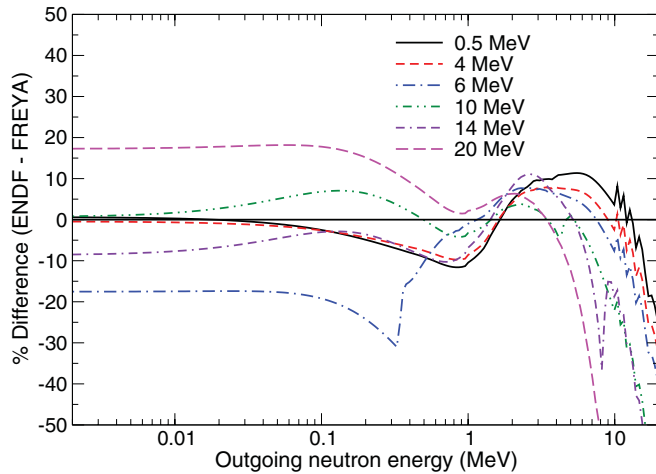


FIG. 13. (Color online) The percent difference between the ENDF-B/VII.0 evaluation of the PFNS and our result when the PFNS data are included in the fit. Results are shown for 0.5 (solid black), 4 (short dashed red), 6 (dot-dashed blue), 10 (dot-dot-dashed green), 14 (dot-dash-dashed violet), and 20 (long dashed magenta) MeV.

than 1% below outgoing energies of 0.1 MeV. There is a transition region between 0.1 and 3 MeV where the percent difference changes sign before the tail region begins. The minimum of the dip at $\sim -10\%$ for $E_n < 4$ MeV indicates that the FREYA spectra have slightly lower average energies. The FREYA evaluation has a higher energy tail than ENDF-B-VII.0 for all E_n . As already noted, the difference is larger for the fit to $\bar{\nu}$ alone, as shown in Fig. 12 for $E > 4$ MeV. The difference is largest for $E_n \leq 4$ MeV where there are spectral data.

As noted in the discussion of Fig. 10, contributions from pre-fission neutron emission change the calculated spectral slope at $E = E_n - S_n$. Although the Madland-Nix (Los Alamos model) evaluation [11] includes an average result for multichance fission, the spectral shape for pre-fission emission is assumed to be the same as that of prompt neutron emission (evaporation) postfission. Thus the ENDF-B-VII.0 evaluations are always smooth over the entire outgoing energy regime, regardless of incident energy, while the FREYA evaluations reflect the changes due to pre-fission emission. The slope changes at the multichance fission thresholds in the FREYA spectra are evident for the $E_n = 6, 10,$ and 14 MeV difference curves at 0.35, 4.35, and 8.35 MeV, respectively. We note that the threshold at 0.35 MeV is exaggerated because the FREYA spectrum is $\sim 20\%$ higher than ENDF-B/VII.0 in this region. Indeed, the difference is larger here than for all other incident energies below 20 MeV.

Figure 14 shows the ratio of our 0.5 MeV results to a Maxwell distribution with $T = 1.42$ MeV. The ENDF-B/VII.0 ratio is also shown, along with data from Refs. [41–49]. As expected from the comparison in Figs. 12 and 13, the FREYA ratio peaks at a lower energy than the ENDF-B/VII.0 ratio. Because there is a great deal of scatter in the data over the entire energy range, any strong conclusion about the quality of the fits with respect to the spectral data is difficult. We do note, however, that the resulting fit to $\bar{\nu}$ only exhibits a smaller deviation from a Maxwellian for $E > 4$ MeV

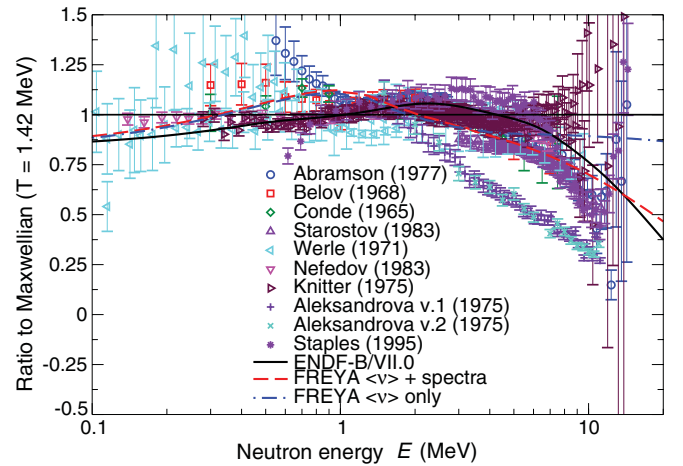


FIG. 14. (Color online) The ratios of ENDF-B/VII.0 (solid) and FREYA fit to $\bar{\nu}$ only (dot-dashed) and including the spectral data (long dashed) relative to a Maxwell distribution with $T = 1.42$ MeV. The data from Refs. [41–49] are also shown relative to the same Maxwellian.

C. Covariances

We can calculate covariances and correlation coefficients between the optimal model parameter values as well as between the various output quantities using Eq. (26). The covariance between two parameters m_k and $m_{k'}$ is

$$\Sigma_{kk'} \equiv \langle (m_k - \langle m_k \rangle)(m_{k'} - \langle m_{k'} \rangle) \rangle. \quad (29)$$

The diagonal elements, Σ_{kk} are the variances $(\Delta m_k)^2$, representing the squares of the uncertainty on the optimal value of the individual model parameter m_k , while the off-diagonal elements give the covariances between two different model parameters. It is often more instructive to employ the associated *correlation coefficients*, $C_{kk'} \equiv \Sigma_{kk'}/[\Sigma_{m_k} \Sigma_{m_{k'}}]$, which is plus (minus) one for fully (anti)correlated variables and vanishes for entirely independent variables.

When only $\bar{\nu}$ is included in the fit, the d TKE correlations, $C_{d\text{TKE}(E_n), d\text{TKE}(E_n)}$, are fairly large except for those with $E_n = 20$ MeV where $\bar{\nu}$ is not well known. In this case, they are weakly anticorrelated. The e_0 - d TKE coefficients, $C_{e_0, d\text{TKE}(E_n)}$, exhibit a relatively strong anticorrelation except at 20 MeV where there is a weak correlation. The x - d TKE coefficients, $C_{x, d\text{TKE}(E_n)}$, show a moderate correlation, $\sim 0.35 - 0.5$, increasing to ~ 0.9 at $E_n = 14$ MeV and becoming weakly anticorrelated at $E_n = 20$ MeV. The correlation coefficient between the energy-independent parameters e_0 and x , $C_{e_0, x}$, is ≈ -0.6 , a rather significant anticorrelation. These results show that similar fits can be obtained by increasing e_0 while decreasing d TKE (or vice versa); changing x and d TKE up and/or down together; or increasing e_0 while decreasing x (or vice versa).

On the other hand, when the spectra are included in the fits, the correlation coefficients are all small and alternating in sign from positive to negative except for $C_{e_0, x}$ which is equivalent to the value for the fit to $\bar{\nu}$ alone. These results suggest that, in this case, the inputs are essentially uncorrelated.

We may also compute the covariance between the spectral strength at different outgoing energies E using Eq. (26). The

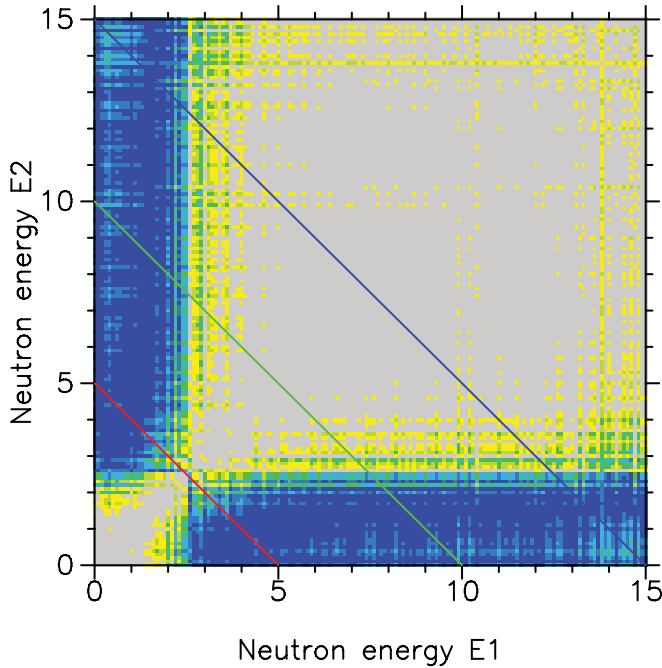


FIG. 15. (Color online) Contour plot of the correlation coefficient [see Eq. (26)] between the spectral strengths at two different energies, C_{E_1, E_2} , as obtained for $E_n = 0.5$ MeV when fitting to \bar{v} only. The correlation changes from values near +1 in the reddish regions (lower left and central regions) to values near -1 in the bluish regions (near the two axes). Each of the three straight lines connects points at which the two neutrons have the same combined energy, $E_1 + E_2 = 5, 10,$ and 15 MeV.

resulting correlation coefficients C_{E_1, E_2} are shown in Figs. 15 and 16 for $E_n = 0.5$ MeV when fitting to \bar{v} alone and including the spectra, respectively. We see that $C_{E_1, E_2} \approx 1$ (gray areas) when the two specified energies lie on the same side of the crossover region, while $C_{E_1, E_2} \approx -1$ (dark blue areas) when they lie on opposite sides. The crossover region around 2.5 MeV indicates that the spectrum tends to pivot around this point when the parameter space is explored, similar to Ref. [6].

The correlation in Fig. 15 is somewhat noisy, especially near the region where C_{E_1, E_2} changes from positive to negative and also where E_1 or E_2 is large and the spectral statistics is poorer. On the other hand, when the spectra are included, $C_{E_1, E_2} > 0$, ~ 0.8 when E_1 and E_2 are similar, gradually decreasing to a very weak anticorrelation when the two energies are very different.

The choice of a BSFG level density parametrization causes larger fluctuations in C_{E_1, E_2} than an energy-independent level density, $a = A/e_0$, as in an average fission model. In this case the temperature is also independent of E_n . Strong correlations are also observed in other calculations based on average fission models such as Madland-Nix [51]. Introducing the BSFG parametrization [Eq. (15)], at fixed U , ignoring the pairing energy, as in our previous paper, introduces fluctuations in a which soften the linear rise of a with A and reduce the sharpness of the correlations. Including the back shift due to the pairing energy further reduces the correlations, narrowing the peak in the spectra. Thus the back shift interferes with the

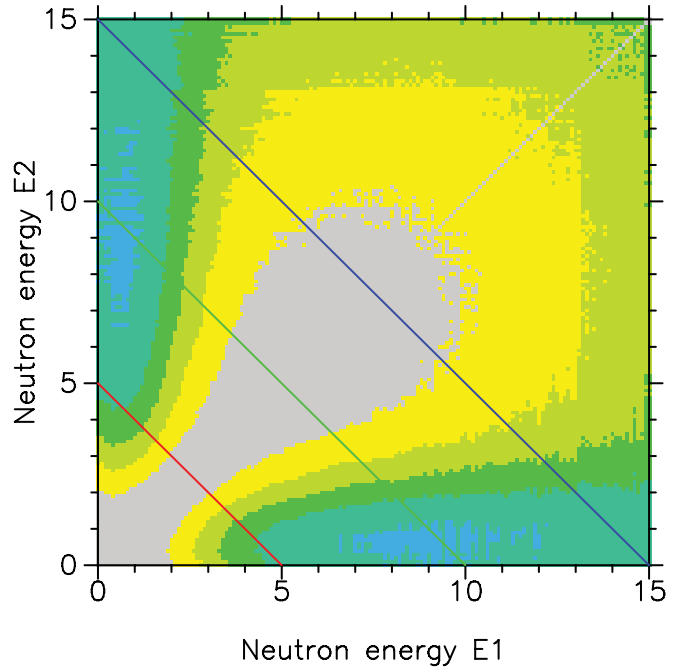


FIG. 16. (Color online) Contour plot of the correlation coefficient [see Eq. (26)] between the spectral strengths at two different energies, C_{E_1, E_2} , as obtained for $E_n = 0.5$ MeV when the spectra are included in the fitting procedure. The correlation changes from values near +1 in the reddish regions (lower left and central regions) to values near -1 in the bluish regions (near the two axes). Each of the three straight lines connects points at which the two neutrons have the same combined energy, $E_1 + E_2 = 5, 10,$ and 15 MeV.

correlations, introducing the noise shown in Fig. 15. Including the spectra in the fits tends to wash out this effect by weakening the overall correlation.

Different correlation matrices are obtained in the two fits. The \bar{v} only fits exhibit increased fluctuations at higher E_n with a wider crossover region between positive and negative C_{E_1, E_2} . In addition, the pivot point moves to slightly higher energies. In the case when the spectra are included in the fits, E_1 and E_2 are correlated over a wider range of ΔE , becoming uncorrelated when E_1 and E_2 are both large.

Figures 17 and 18 show cuts at constant total neutron energy, $E_1 + E_2$. Similar results are found for all other

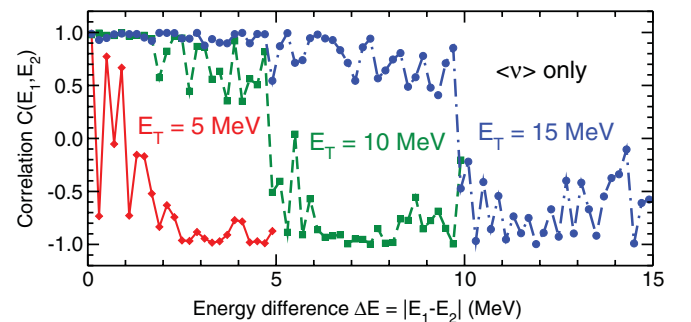


FIG. 17. (Color online) The spectral correlation coefficients, C_{E_1, E_2} , along the three lines of constant combined energy indicated in Fig. 15 for the fit to \bar{v} only at $E_n = 0.5$ MeV.

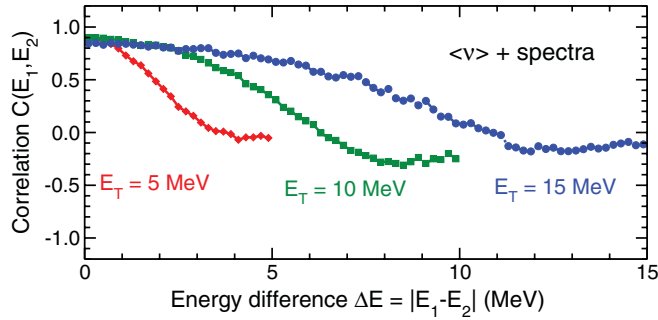


FIG. 18. (Color online) The spectral correlation coefficients, C_{E_1, E_2} , along the three lines of constant combined energy indicated in Fig. 16 for the fit to $\bar{\nu}$ and the spectral data at $E_n = 0.5$ MeV.

incident energies considered. The trends are the same for both scenarios, large positive correlations at low ΔE , becoming negative at larger ΔE . However, the fits with spectra included show almost no correlation, $C_{E_1, E_2} \sim 0$ for large ΔE . When the model parameters are varied in both cases, the spectral shapes pivot about a single energy, $E_{\text{pivot}} \sim 2.5$ MeV in these calculations. Thus when both E_1 and E_2 are less than E_{pivot} , the differential changes are in phase and $C_{E_1, E_2} \sim 1$. If, for example, $E_1 < E_{\text{pivot}}$ and $E_2 > E_{\text{pivot}}$, differential changes in the spectra give an anticorrelation.

IV. BENCHMARK TESTS

There are several standard validation calculations that can be used to test our PFNS evaluations. They are critical assemblies which test conditions under which a fission chain reaction remains stationary, that is, exactly critical; activation ratios which can be used to test the modeling of the flux in a critical assembly; and pulsed sphere measurements which test the spectra for incident neutron energies of ~ 14 MeV.

To perform these tests, we replace the $^{239}\text{Pu}(n, f)$ PFNS in the ENDL2011.0 database, identical to that in ENDF-B/VII.0, with our evaluated spectra. Our evaluation thus has the same format as the ENDF-B/VII.0 evaluation and represents the spectra averaged over all neutron multiplicities. In this section, we describe these tests and the FREYA results.

A. Validation against critical assemblies

Critical assemblies, which are designed to determine the conditions under which a fission chain reaction is stationary, provide an important quality check on the spectral evaluations. The key measure of a critical assembly is the neutron multiplication factor k_{eff} . When this quantity is unity, the assembly is exactly critical, that is, the net number of neutrons does not change so that for every neutron generated, another is either absorbed or leaks out of the system. For a given assembly, the degree of criticality depends on the multiplicity of prompt neutrons, their spectral shape, and the energy-dependent cross section for neutron-induced fission.

Plutonium criticality is especially sensitive to the prompt neutron spectrum because the $^{239}\text{Pu}(n, f)$ cross section rises sharply between $E_n = 1.5$ and 2 MeV, near the peak of the fission spectrum. As a result, increasing the relative number

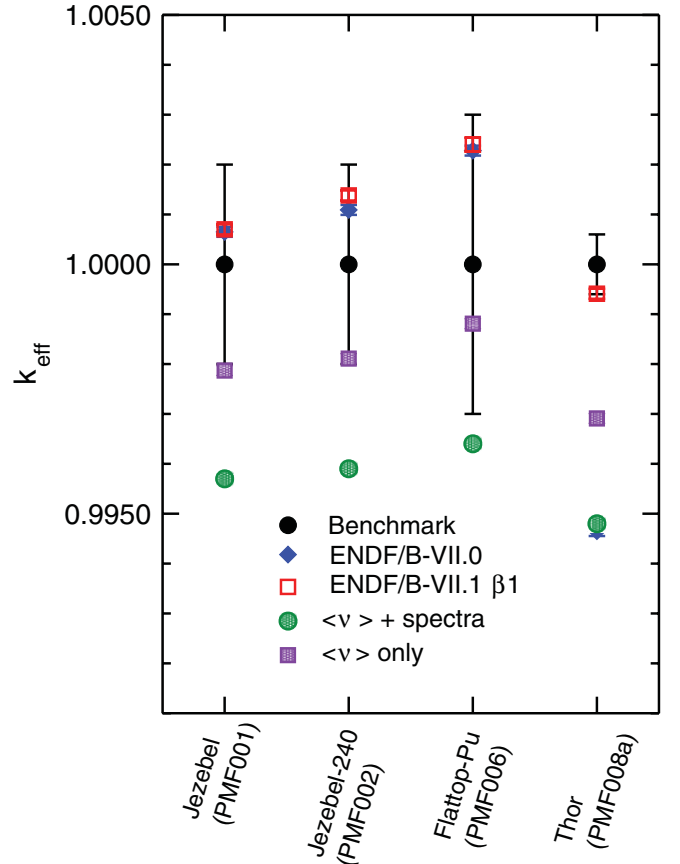


FIG. 19. (Color online) Calculated values of k_{eff} for several ^{239}Pu critical assemblies obtained using our fits to $\bar{\nu}$ only (solid violet squares) and fits to $\bar{\nu}$ and the spectra (solid green circles) in the Mercury code. The results are compared to calculations using the ENDF-B/VII.0 (blue diamonds) and proposed ENDF-B-VII.1 (open red squares) databases.

of low-energy neutrons tends to decrease criticality, lowering k_{eff} , while increasing the number of higher energy neutrons increases criticality.

Figure 19 shows calculations of k_{eff} for four different plutonium assemblies from the criticality safety benchmark handbook [52]. Apart from the spectra, all data used in these calculations were taken from ENDF-B-VII.0 [8]. We show the k_{eff} for the two fits with our evaluated spectra and $\bar{\nu}$ from the ENDF-B/VII.0 evaluation. The value of k_{eff} is significantly below the reported uncertainties on the assemblies while the fit to $\bar{\nu}$ alone is typically within one standard deviation of the measured value.

The energy-independent result of Ref. [6] led to values of k_{eff} that were ≈ 1.5 standard deviations away from the measured value for the Jezebel assembly which is sensitive to fission induced by fast ($E_n \approx 1$ MeV) neutrons. By contrast, our results fitting to $\bar{\nu}$ alone thus represent some improvement.

We note that the other inputs to the Jezebel assembly test were highly tuned to match the k_{eff} . The fact that replacing only the PFNS without a full reevaluation of all the inputs to the criticality tests leads to a result that is inconsistent with

$k_{\text{eff}} \equiv 1$ should therefore not be surprising. For example, if the average energy of the ENDF-B/VII.0 PFNS is high, the \bar{v} evaluation would be forced higher to counter the effect on k_{eff} . In addition, the inelastic (n, n') cross section is not well known and could require compensating changes that affect k_{eff} [53].

To make further improvements in the evaluations with respect to assemblies, it would be useful to have an inline version of FREYA for use in the simulations.

B. Validation against activation ratios

In the 1970s and 1980s, LANL performed a series of experiments using the spectra from the critical assemblies Jezebel (mainly ^{239}Pu), Godiva, BigTen, and Flatop25 (all primarily enriched uranium) to activate foils of various materials [54]. The isotopic content of the foils can be radiochemically assessed both before and after irradiation. Thus these measurements of the numbers of atoms produced per fission neutron are an integral test of specific reaction cross sections in the foil material. Conversely, a well-characterized material can also be used to test the critical assembly flux modeling. We have simulated several foils (^{239}Pu , ^{233}U , ^{235}U , ^{238}U , ^{237}Np , ^{51}V , ^{55}Mn , ^{63}Cu , ^{93}Nb , ^{107}Ag , ^{121}Sb , ^{139}La , ^{193}Ir , and ^{197}Au) which are tests of the (n, f) and (n, γ) reactions in the Jezebel assembly. In all cases, our simulated values of the activation rates in these foils are either consistent with measured values or previous modeling using a modified version of the ENDF/B-VII.0 nuclear data library [55]. As the fission cross sections for ^{233}U , ^{235}U , ^{238}U , and ^{237}Np are accurately known and span all incident neutron energies, these tests merely confirm our earlier modeling of plutonium critical assemblies. The neutron capture cross sections of the other foils are important for incident neutron energies less than 1 MeV but they are not known nearly as well as the fission cross sections. Thus our Calculated/Experiment ratios scatter around unity in these cases.

Because both the Jezebel and Godiva critical assemblies test the fast-neutron spectrum, with a significant portion of their neutron fluxes above 5 MeV, either might be used to test the high-energy portion of the $^{239}\text{Pu}(n, f)$ PFNS. Unfortunately, none of the tests that have been performed to date are useful for testing our FREYA PFNS evaluation. While many of the studied materials have high (≥ 10 MeV) $(n, 2n)$ thresholds, the only $(n, 2n)$ threshold material tested in Jezebel is ^{169}Tm . Unfortunately, the $^{169}\text{Tm}(n, 2n)$ cross section is poorly known. There were also experiments with plutonium foils placed in uranium assemblies, but these tests are not useful for testing the $^{239}\text{Pu}(n, f)$ PFNS because the foils are too thin for secondary scatterings to play a significant role. It would be particularly interesting to carry out a new set of $(n, 2n)$ foil measurements using well-characterized materials in a primarily plutonium critical assembly to specifically test the high-energy portion of the spectrum.

C. Validation with LLNL pulsed spheres

The ENDL2011.0 database [56], including our FREYA evaluation, was tested against LLNL pulsed-sphere data, a

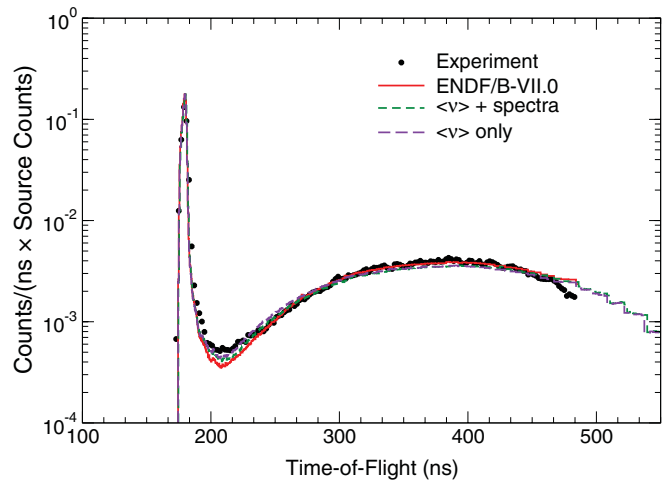


FIG. 20. (Color online) The measured LLNL pulsed-sphere test data [58] (points) compared to calculations using either ENDF/B-VII.0 or ENDL2011.0 with the present FREYA evaluation included.

set of fusion-shielding benchmarks [57]. The pulsed-sphere program, which ran from the 1970s to the early 1990s, measured neutron time-of-flight (TOF) and gamma spectra resulting from emission of a 14 MeV neutron pulse produced by $d + t$ reactions occurring inside spheres composed of a variety of materials [58]. Models of the LLNL pulsed-sphere experiments using the Mercury Monte Carlo were developed for the materials reported in Goldberg *et al.* [59,60].

Figure 20 compares results of our evaluation with the experimental data [58] and calculations based on ENDF/B-VII.0. The only difference between the Pu evaluations in these two calculations is the PFNS and associated \bar{v} , all other quantities remain the same. Relative to the ENDF/B-VII.0 calculation, in both cases the FREYA spectra yields better agreement with the data in the region around the minimum of the time-of-flight curve at ≈ 210 ns and up to ≈ 300 ns. However, it lies somewhat lower than the ENDF/B-VII.0 curve and the data over the plateau region for time of flight longer than 300 ns.

Such pulsed-sphere experiments test the PFNS at incident energies higher than those probed in critical assembly tests. The measured outgoing neutrons have a characteristic time-of-flight curve (see Fig. 20). The sharp peak at early times is due to 14 MeV neutrons going straight through the material without significant interaction. The dip at around 200 ns and the rise immediately afterward is caused by secondary scattering in the material as the neutrons travel out from the center. The location and depth of the dip is due to inelastic direct reactions, the high-energy tail of the prompt fission neutron spectrum, and pre-equilibrium neutron emission. The last two items are directly addressed by the present evaluation. A large part of the secondary interactions are due to neutrons that have interacted in the material and are thus less energetic than those from the initial 14 MeV pulse. At late times, where the results from both evaluations deviate from the data, the time-of-flight spectrum is dominated by scattering in surrounding material such as detector components and concrete shielding.

D. Additional observables

The mass-averaged fragment kinetic energies obtained with FREYA are almost independent of the incident neutron energy E_n . This feature is consistent with measurements made with ^{235}U and ^{238}U targets over similar ranges of incident neutron energy, $0.5 \leq E_n \leq 6$ MeV [19] and $1.2 \leq E_n \leq 5.8$ MeV [61], respectively. In both cases, the average TKE changes less than 1 MeV over the entire energy range.

However, Ref. [61] also showed that, while the mass-averaged TKE is consistent with near energy independence, higher energy incident neutrons typically give less TKE to masses close to symmetric fission and somewhat more TKE for $A_H > 140$. Such detailed information is not available for neutrons on ^{239}Pu . We have therefore chosen to use a constant value of $d\text{TKE}$ at each energy.

Neutron observables are perhaps more useful for model validation. The near independence of $\text{TKE}(A_H)$ on incident energy implies that the additional energy brought into the system by a more energetic neutron will be primarily converted into internal excitation energy. This is illustrated in the top panel of Fig. 21 which shows the fragment excitation $E^*(A_f)$

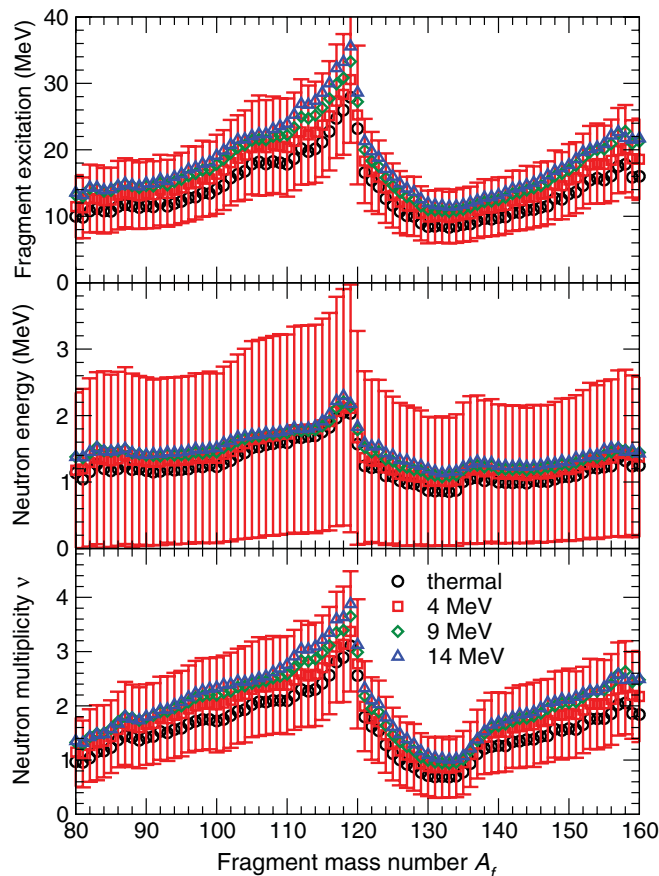


FIG. 21. (Color online) The total average excitation energy available for neutron emission (top), the average neutron kinetic energy (middle), and the average neutron multiplicity (bottom) as a function of fragment mass number A_f for thermal neutrons (black circles), $E_n = 4$ (red squares), 9 (green diamonds), and 14 (blue triangles) MeV. Here the FREYA dispersion on each A_f is only shown for $E_n = 4$ MeV to simplify the plots.

for the representative incident energies considered in Fig. 10 (thermal, 4, 9, and 14 MeV): $E^*(A_f)$ increases linearly with incident energy. We note that the form of $\text{TKE}(A_H)$ (see Fig. 5) leads to the familiar sawtooth form of $E^*(A_f)$.

The average kinetic energy of the evaporated neutrons is given by $\bar{E} = 2T$ for a single emission, where T is the maximum temperature in the daughter nucleus, so $T^2 \propto E^* - S_n$ for the first emission. Consequently, \bar{E} should vary relatively little with A_f , as is indeed borne out by the results for $\bar{E}(A_f)$ shown in the middle panel of Fig. 21. The average outgoing neutron kinetic energy increases slowly with the incident neutron energy, with a total increase of $\approx 20\%$ through the energy range shown. While the ratio σ_E/\bar{E} is $1/\sqrt{2}$ for a single neutron emission, the ratio grows with E_n due to multiple neutron emission and the consequent appearance of spectral components with differing degrees of hardness.

The relatively flat behavior of $\bar{E}(A_f)$ implies that the neutron multiplicity $\bar{\nu}(A_f)$ will resemble the fragment excitation energy $E^*(A_f)$, as is seen to be the case in the bottom panel of Fig. 21 where the characteristic sawtooth shape of $\bar{\nu}(A_f)$ is apparent. The number of neutrons from the heavy fragment

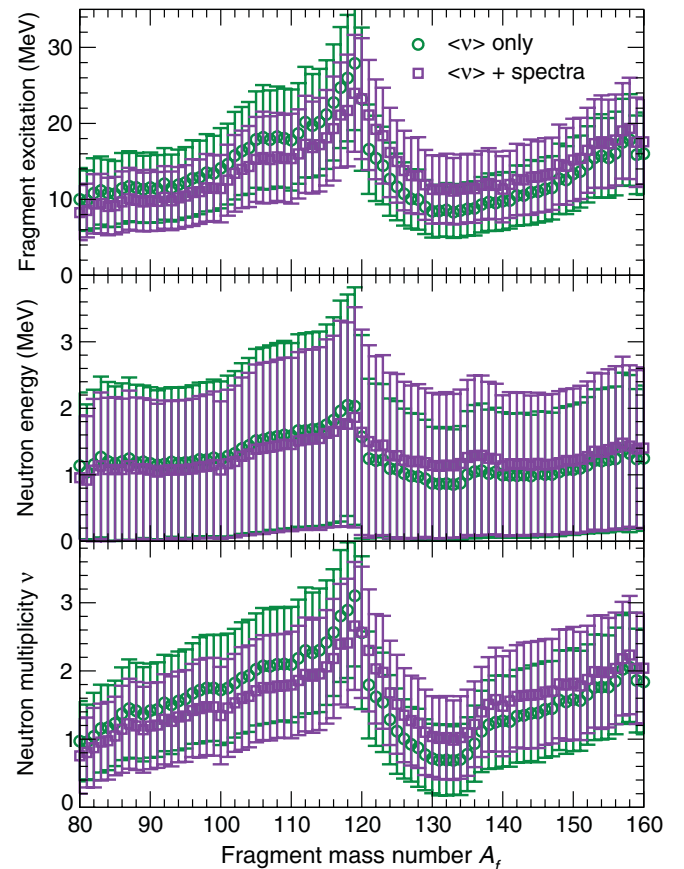


FIG. 22. (Color online) The total average excitation energy available for neutron emission (top), the average neutron kinetic energy (middle), and the average neutron multiplicity (bottom) as a function of fragment mass number A_f for $E_n = 0.5$ MeV. The fit results are shown for $\bar{\nu}$ only (circles) and with the spectra included (squares). The calculated dispersion for each value of A_f is also shown.

increases somewhat faster with E_n than the number from the light fragment.

Figure 22 shows the fragment excitation energy E^* , the kinetic energy of the emitted neutron and the neutron multiplicity, all as a function of A_f for the two fits at $E_n = 0.5$ MeV. The larger x of the $\bar{\nu}$ only fit gives both a stronger dependence of E^* on A_f and a sharper “sawtooth” shape. The neutron kinetic energy is not strongly affected by the value of x .

New measurements with the fission TPC [62] over a range of incident neutron energies could provide a wealth of data that could lead to improved modeling. In addition, calculations of “hot” fission that includes temperature-dependent shell effects could enhance modeling efforts by predicting trends that could be input into FREYA and thus test the effects on the PFNS and related quantities.

For reasons of computational simplicity, we have chosen to use the same value of x over the entire energy range considered. There are some limited data on thermal neutron-induced fission of ^{235}U [33] and spontaneous fission of ^{252}Cf [34] that suggest the light fragment emits more neutrons than the heavy fragment, 40% more for ^{235}U [33] and 20% more for ^{252}Cf [34]. Our fit to $\bar{\nu}$ only, $x \sim 1.24$, is consistent with these results. However, “hotter” fission could equilibrate the excitation energies of the light and heavy fragments which may result in more neutron emission from the heavy fragment, also reducing the sharpness of the sawtooth pattern.

Figure 23 shows the neutron multiplicity distribution $P(\nu)$ for the selected values of E_n . As expected, $\bar{\nu}$ increases with E_n and the distribution broadens. However, each neutron reduces the excitation energy in the residue by not only its kinetic energy (recall $\bar{E} = 2T$) but also by the separation energy S_n (which is generally significantly larger). Therefore the resulting $P(\nu)$ is narrower than a Poisson distribution with the same average multiplicity.

The combined kinetic energy of the two resulting (postevaporation) product nuclei is shown as a function of the neutron multiplicity ν in the top panel of Fig. 24. It decreases with increasing multiplicity, as one might expect on the grounds

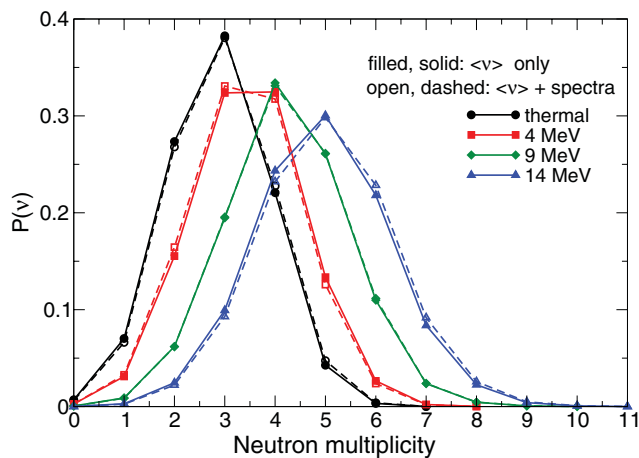


FIG. 23. (Color online) The neutron multiplicity distribution obtained for thermal neutrons (black circles), $E_n = 4$ (red squares), 9 (green diamonds), and 14 (blue triangles) MeV.

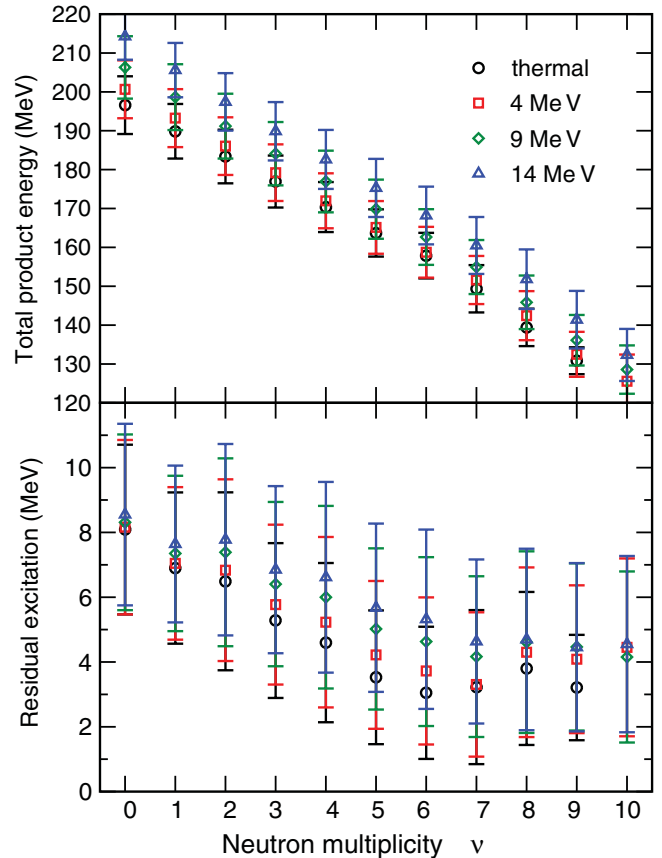


FIG. 24. (Color online) The combined kinetic energy of the two product nuclei (top) and their residual excitation prior to photon emission (bottom) as functions of the neutron multiplicity ν for thermal neutrons and $E_n = 4, 9$, and 14 MeV. The symbols are at the mean values and the vertical bars show the dispersions of the respective distributions for each value of the multiplicity.

that the emission of more neutrons tends to require more initial excitation energy, thus leaving less available for fragment kinetic energy.

The bottom panel of Fig. 24 shows the mass dependence of the average residual excitation energy in those postevaporation product nuclei. Because energy is available for the subsequent photon emission, one may expect that the resulting photon multiplicity would display a qualitatively similar behavior and thus, in particular, be anticorrelated with the neutron multiplicity. These results show little sensitivity to the fit method.

V. CONCLUSION

We have included both multichance fission and pre-equilibrium neutron emission into FREYA [6,7], a Monte Carlo model that simulates fission on an event-by-event basis. This has enabled us to perform an extended evaluation of the prompt fission neutron spectrum from $^{239}\text{Pu}(n, f)$ up to $E_n = 20$ MeV. Several physics-motivated model parameters have been fitted to the ENDF-B/VII.0 evaluation of $\bar{\nu}$ and the associated

covariance matrix in two alternate scenarios for the level-density parametrization.

The tests of our evaluation were inconclusive. Our evaluation did not perform as well as the ENDF/B-VII.0 evaluation in critical assembly benchmarks. However, we found improved agreement with the LLNL pulsed sphere tests, especially just below the 14 MeV peak in the neutron leakage spectrum. Although these mixed results may limit the utility of our evaluation in applications, they do give us hope that further improvements to the evaluation will either tighten up agreement with the critical assemblies or point to other deficiencies in the ENDF-B/VII.0 ^{239}Pu evaluation.

Further investigations will require fitting to other data less sensitive to the $\bar{\nu}$ data employed in this work including the albeit low-quality PFNS data and $\bar{\nu}(A)$ data. Such data may be obtained from new fragment mass, charge, and

TKE measurements with the fission TPC [62] or high-quality neutron spectral data to augment or replace older measurements.

ACKNOWLEDGMENTS

We acknowledge many helpful discussions with R. Capote Noy, M. Chadwick, D. Heinrichs, T. Kawano, P. Möller, J. Pruet, W. J. Swiatecki, P. Talou, M. White, and W. Younes. This work was performed under the auspices of the US Department of Energy by Lawrence Livermore National Laboratory under Contract No. DE-AC52-07NA27344 (R.V., D.B., M.A.D., W.E.O.) and Lawrence Berkeley National Laboratory under Contract No. DE-AC02-05CH11231 (J.R.), and was also supported in part by the National Science Foundation Grant No. NSF PHY-0555660 (R.V.).

-
- [1] P. Möller, D. G. Madland, A. J. Sierk, and A. Iwamoto, *Nature (London)* **409**, 785 (2001).
- [2] P. Möller, A. J. Sierk, T. Ichikawa, A. Iwamoto, R. Bengtsson, H. Uhrenholt, and S. Åberg, *Phys. Rev. C* **79**, 064304 (2009).
- [3] J.-F. Berger, M. Girod, and D. Gogny, *Nucl. Phys. A* **428**, 23 (1984).
- [4] H. Goutte, J.-F. Berger, P. Casoli, and D. Gogny, *Phys. Rev. C* **71**, 024316 (2005).
- [5] N. Dubray, H. Goutte, and J.-P. Delaroche, *Phys. Rev. C* **77**, 014310 (2008).
- [6] R. Vogt, J. Randrup, J. Pruet, and W. Younes, *Phys. Rev. C* **80**, 044611 (2009).
- [7] J. Randrup and R. Vogt, *Phys. Rev. C* **80**, 024601 (2009).
- [8] M. B. Chadwick, P. Obložinský, M. Herman, N. M. Greene, R. D. McKnight, D. L. Smith, P. G. Young, R. E. MacFarlane, G. M. Hale, S. C. Frankle, A. C. Kahler, T. Kawano, R. C. Little, D. G. Madland, P. Moller, R. D. Mosteller, P. R. Page, P. Talou, H. Trellue, M. C. White, W. B. Wilson, R. Arcilla, C. L. Dunford, S. F. Mughabghab, B. Pritychenko, D. Rochman, A. A. Sonzogni, C. R. Lubitz, T. H. Trumbull, J. P. Weinman, D. A. Brown, D. E. Cullen, D. P. Heinrichs, D. P. McNabb, H. Derrien, M. E. Dunn, N. M. Larson, L. C. Leal, A. D. Carlson, R. C. Block, J. B. Briggs, E. T. Cheng, H. C. Huria, M. L. Zerkle, K. S. Kozier, A. Courcelle, V. Pronyaev, and S. C. van der Marck, *Nucl. Data Sheets* **107**, 2931 (2006).
- [9] W. J. Swiatecki, K. Siwek-Wilczynska, and J. Wilczynski, *Phys. Rev. C* **78**, 054604 (2008).
- [10] T. Kawano, T. Ohsawa, M. Baba, and T. Nakagawa, *Phys. Rev. C* **63**, 034601 (2001).
- [11] D. G. Madland and J. R. Nix, *Nucl. Sci. Eng.* **81**, 213 (1982).
- [12] E. Gadioli and P. E. Hodgson, *Pre-equilibrium Nuclear Reactions* (Oxford University Press, New York, 1992).
- [13] A. J. Koning and M. C. Duijvestijn, *Nucl. Phys. A* **744**, 15 (2004).
- [14] J. Dobeš and E. Běták, *Z. Phys. A* **310**, 329 (1983).
- [15] A. J. Koning and J. P. Delaroche, *Nucl. Phys. A* **713**, 231 (2003).
- [16] W. Younes, J. A. Becker, L. A. Bernstein, P. E. Garrett, C. A. McGrath, D. P. McNabb, R. O. Nelson, G. D. Johns, W. S. Wilburn, and D. M. Drake, *Phys. Rev. C* **64**, 054613 (2001).
- [17] U. Brosa, S. Grossmann, and A. Müller, *Phys. Rep.* **97**, 1 (1990); U. Brosa, *Phys. Rev. C* **32**, 1438 (1985).
- [18] T. R. England and B. F. Rider, Los Alamos National Laboratory Report No. LA-UR-94-3106, 1994.
- [19] F.-J. Hamsch, H. H. Knitter, C. Budtz-Jørgensen, and J. P. Theobald, *Nucl. Phys. A* **491**, 56 (1987).
- [20] L. E. Glendenin, J. E. Gindler, D. J. Henderson, and J. W. Meadows, *Phys. Rev. C* **24**, 2600 (1981).
- [21] J. E. Gindler, L. E. Glendenin, D. J. Henderson, and J. W. Meadows, *Phys. Rev. C* **27**, 2058 (1983).
- [22] W. Reisdorf, J. P. Unik, H. C. Griffin, and L. E. Glendenin, *Nucl. Phys. A* **177**, 337 (1971).
- [23] G. Audi and A. H. Wapstra, *Nucl. Phys. A* **595**, 409 (1995).
- [24] P. Möller, J. R. Nix, W. D. Myers, and W. J. Swiatecki, *At. Data Nucl. Data Tables* **59**, 185 (1995).
- [25] B. D. Wilkins, E. P. Steinberg, and R. R. Chasman, *Phys. Rev. C* **14**, 1832 (1976).
- [26] C. Wagemans, E. Allaert, A. Deruytter, R. Barthélémy, and P. Schillebeeckx, *Phys. Rev. C* **30**, 218 (1984).
- [27] K. Nishio, Y. Nakagome, I. Kanno, and I. Kimura, *J. Nucl. Sci. Technol.* **32**, 404 (1995).
- [28] C. Tsuchiya, Y. Nakagome, H. Yamana, H. Moriyama, K. Nishio, I. Kanno, K. Shin, and I. Kimura, *J. Nucl. Sci. Technol.* **37**, 941 (2000).
- [29] V. F. Apalin, Yu. N. Gritsyuk, I. E. Kutikov, V. I. Lebedev, and L. A. Mikaelian, *Nucl. Phys. A* **71**, 553 (1965).
- [30] T. Kawano (private communication).
- [31] S. Lemaire, P. Talou, T. Kawano, M. B. Chadwick, and D. G. Madland, *Phys. Rev. C* **72**, 024601 (2005).
- [32] H. Koura, M. Uno, T. Tachibana, and M. Yamada, *Nucl. Phys. A* **674**, 47 (2000).
- [33] K. Nishio, Y. Nakagome, H. Yamamoto, and I. Kimura, *Nucl. Phys. A* **632**, 540 (1998).
- [34] A. S. Vorobyev, V. N. Dushin, F. J. Hamsch, V. A. Jakovlev, V. A. Kalinin, A. B. Laptev, B. F. Petrov, and O. A. Shcherbakov, in *Proceedings of the International Conference on Nuclear Data for Science and Technology, ND2004, Santa Fe, New Mexico* (AIP Conference Proceedings, Melville, 2004).
- [35] S. Lemaire, P. Talou, T. Kawano, M. B. Chadwick, and D. G. Madland, *Phys. Rev. C* **73**, 014602 (2006).
- [36] V. F. Weisskopf, *Phys. Rev.* **52**, 295 (1937).

- [37] A. Tarantola, *Inverse Problem Theory* (SIAM Press, Philadelphia, 2005).
- [38] M. D. McKay, R. J. Beckman, and W. J. Conover, *Technometrics* **21**, 239 (1979).
- [39] R. L. Iman, J. C. Helton, and J. E. Campbell, *Journal of Quality Technology* **13**, 174 (1981).
- [40] P. G. Young, M. B. Chadwick, R. E. MacFarlane, P. Talou, T. Kawano, D. G. Madland, W. B. Wilson, and C. W. Wilkerson, *Nucl. Data Sheets* **108**, 2589 (2007).
- [41] D. Abramson and C. Lavelaine, Atomic Energy Research Establishment Report No. 8636, Harwell, 1977 [<http://www-nds.iaea.org/exfor/servlet/X4sGetSubent?subID=20997004>].
- [42] L. M. Belov, M. V. Blinov, N. M. Kazarinov, A. S. Krivokhatskij, and A. N. Protopopov, *Yad.-Fiz. Issl. Rep.* **6**, 94 (1968).
- [43] H. Conde and G. During, *Arkiv för Fysik* **29**, 313 (1965).
- [44] B. I. Starostov, V. N. Nefedov, and A. A. Bojcov, in *Proceedings of 6th All-Union Conference on Neutron Physics, Kiev, Ukraine*, Vol. 2 (IAEA, Vienna, 1983), p. 290.
- [45] H. Werle and H. Bluhm, in *Prompt Fission Neutron Spectra Meeting* (IAEA, Vienna, 1971), p. 65.
- [46] V. N. Nefedov, B. I. Starostov, and A. A. Bojcov, in *Proceedings of 6th All-Union Conference on Neutron Physics, Kiev, Ukraine*, Vol. 2 (IAEA, Vienna, 1983), p. 285.
- [47] H. Knitter, *Atomkernenerg.* **26**, 76 (1975).
- [48] Z. A. Aleksandrova, V. I. Bol Shov, V. F. Kuznetsov, G. N. Smirenkin, and M. Z. Tarasko, *At. Energ.* **38**, 108 (1975).
- [49] P. Staples, J. J. Egan, G. H. R. Kegel, A. Mittler, and M. L. Woodring, *Nucl. Phys. A* **591**, 41 (1995).
- [50] R. Capote, M. Herman, P. Obložinský, P. G. Young, S. Goriely, T. Belgia, A. V. Ignatyuk, A. J. Koning, S. Hilaire, V. A. Plujko, M. Avrigeanu, O. Bersillon, M. B. Chadwick, T. Fukahori, Z. Ge, Y. Han, S. Kailas, J. Kopecky, V. M. Maslov, G. Reffo, M. Sin, E. Sh. Soukhovitskii, and P. Talou, *Nucl. Data Sheets* **110**, 3107 (2009).
- [51] P. Talou, T. Kawano, D. G. Madland, A. C. Kahler, D. K. Parsons, M. C. White, R. C. Little, and M. B. Chadwick, *Nucl. Sci. Eng.* **166**, 254 (2010).
- [52] B. Briggs, Nuclear Energy Agency Report No. NEA/NSC/DOC(95), Issy-les-Moulineaux, 2006.
- [53] R. Capote (private communication).
- [54] C. Wilkerson, M. Mac Innes, D. Barr, H. Trellue, R. MacFarlane, and M. Chadwick, in *International Conference on Nuclear Data for Science and Technology, Nice, France, April 22–27, 2007* (EDP Sciences, Les Ulis, 2007); B. Briggs, in *International Handbook of Evaluated Critical Safety Benchmark Experiments*, Nuclear Energy Agency Technical Report No. NEQ/NSC/DOC(95), Paris, 2006.
- [55] B. Beck *et al.*, Lawrence Livermore National Laboratory Report No. LLNL-TR-452511, Livermore, 2010.
- [56] D. A. Brown, M.-A. Descalle, J. Escher, R. Hoffman, T. Luu, C. M. Mattoon, P. Navratil, G. Nobre, W. E. Ormand, S. Quaglioni, N. C. Summers, I. J. Thompson, R. Vogt, and R. Barnowski (unpublished).
- [57] M.-A. Descalle and J. Pruet, Lawrence Livermore National Laboratory Report No. LLNL-TR-404630, 2008.
- [58] C. Wong, J. D. Anderson, P. Brown, L. F. Hansen, J. L. Kammerdiener, C. Logan, and B. A. Pohl, Lawrence Livermore National Laboratory Report No. UCRL-51144, Rev. 1, Livermore, 1972.
- [59] E. Goldberg, L. F. Hansen, T. T. Komoto, B. A. Pohl, R. J. Howerton, R. E. Dye, E. F. Plechaty, and W. E. Warren, *Nucl. Sci. Eng.* **105**, 319 (1990).
- [60] A. Marchetti and G. W. Hedstrom, Lawrence Livermore National Laboratory Report No. UCRL-ID-131461, Livermore, 1998.
- [61] F. Vivès, F.-J. Hamsch, H. Bax, and S. Oberstedt, *Nucl. Phys. A* **662**, 63 (2000).
- [62] M. Heffner, *AIP Conf. Proc.* **1005**, 182 (2008).